# Journal Pre-proof


Modelling of hybrid biocomposites for automotive structural applications

Ahmed Elmasry, Wiyao Azoti, Engy Ghoniem, Ahmed Elmarakbi

PII: S0266-3538(24)00132-5

DOI: https://doi.org/10.1016/j.compscitech.2024.110562

Reference: CSTE 110562

To appear in: *Composites Science and Technology*

Received Date: 10 October 2023

Revised Date: 10 February 2024

Accepted Date: 19 March 2024

Please cite this article as: Elmasry A, Azoti W, Ghoniem E, Elmarakbi A, Modelling of hybrid biocomposites for automotive structural applications, *Composites Science and Technology* (2024), doi: https://doi.org/10.1016/j.compscitech.2024.110562.

# Modelling of Hybrid Biocomposites for Automotive Structural Applications

**Ahmed Elmasry[1,2,*], Wiyao Azoti[3], Engy Ghoniem[1,2], Ahmed Elmarakbi[1]**

[1] Faculty of Engineering and Environment, Northumbria University, Newcastle upon Tyne, NE1.8ST, UK

[2] Faculty of Engineering, Alexandria University, Alexandria, 21544 ElHoriya Street, Egypt

[3] Clément Ader Institute (ICA), Federal University Toulouse Midi-Pyrénées, UMR CNRS 5312, INSA, ISAE-SUPAERO, IMT Mines Albi, UPS, 3 rue Caroline Aigle, 31400 Toulouse, France

* Corresponding Author, E-mail: ahmed2.elmasry@northumbria.ac.uk

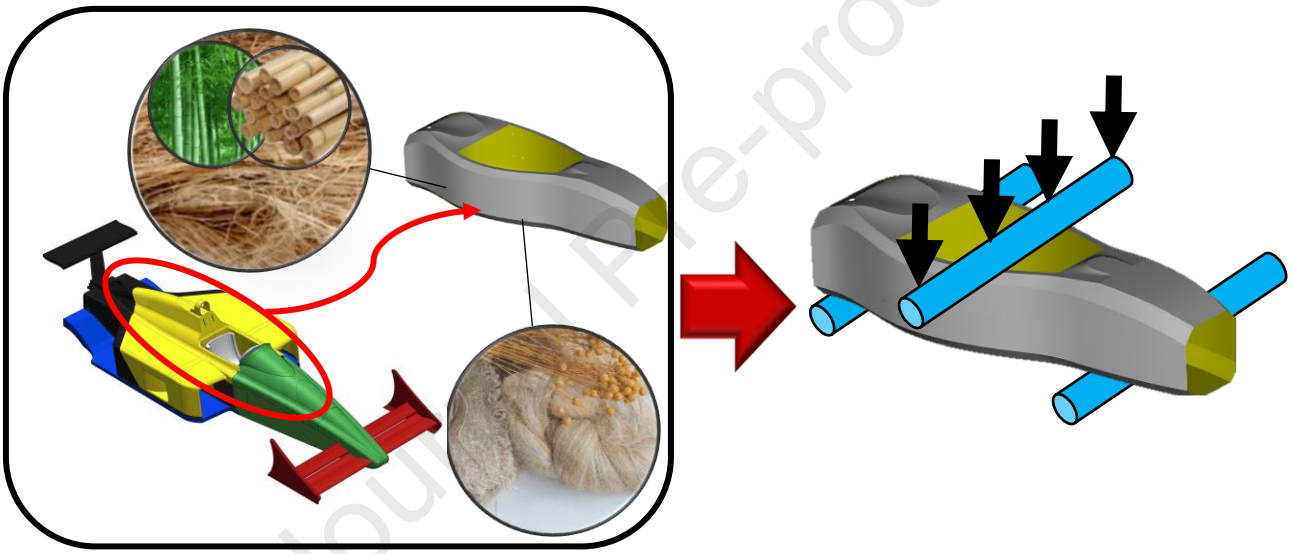



## *Graphical abstract*

# Modelling of Hybrid Biocomposites for Automotive Structural Applications

**Ahmed Elmasry[1,2,*], Wiyao Azoti[3], Engy Ghoniem[1,2], Ahmed Elmarakbi[1]**

[1] Faculty of Engineering and Environment, Northumbria University, Newcastle upon Tyne, NE1.8ST, UK

[2] Faculty of Engineering, Alexandria University, Alexandria, 21544 ElHoriya Street, Egypt

[3] Clément Ader Institute (ICA), Federal University Toulouse Midi-Pyrénées, UMR CNRS 5312, INSA, ISAE-SUPAERO, IMT Mines Albi, UPS, 3 rue Caroline Aigle, 31400 Toulouse, France

* Corresponding Author, E-mail: ahmed2.elmasry@northumbria.ac.uk

## Abstract

The demand for environmentally friendly materials is at its peak, and government legislations have become stricter and no longer tolerate violations. With biocomposites emerging as structural components instead of being hidden as non-structural applications and interiors, the automotive and motorsport sector started considering them for structural body parts. Natural fibres abundance, commercial availability, renewability, low density, low cost, and high tensile strength make biocomposite materials excellent candidates for eco-friendly vehicles. Several studies reported the utilisation of biocomposites as high-performance components and structural applications. However, current computer-aided engineering and modelling tools are insufficient to explore the vast field of possibilities during biocomposite materials selection to accurately predict the components' behaviour and analyses. Therefore, this study focuses on creating a material model to predict the behaviour of biocomposite materials. Additionally, the model is numerically implemented to illustrate the deformation and bending stiffness capabilities of a motorsport monocoque chassis structure application. A micromechanics modelling combining rate-dependant constitutive laws and multi-site interactions of inclusions is developed for studying the nonlinear response of composite materials. To avoid numerical instabilities when increments of time become very small, a regulation procedure concerning the visco-plastic function is adopted in the computation of the consistent tangent modulus. Based on the Generalised Mori–Tanaka (GMT) scheme, the effective properties are obtained for the nonlinear composite. The accuracy of the model is evaluated and validated by comparison results from the open literature. Finally, the developed constitutive equations are implemented as a user-defined material UMAT in a Finite Element code, leading to an application on a bio-based composite for the bamboo/flax fibre-reinforced epoxy hybrid composite materials.

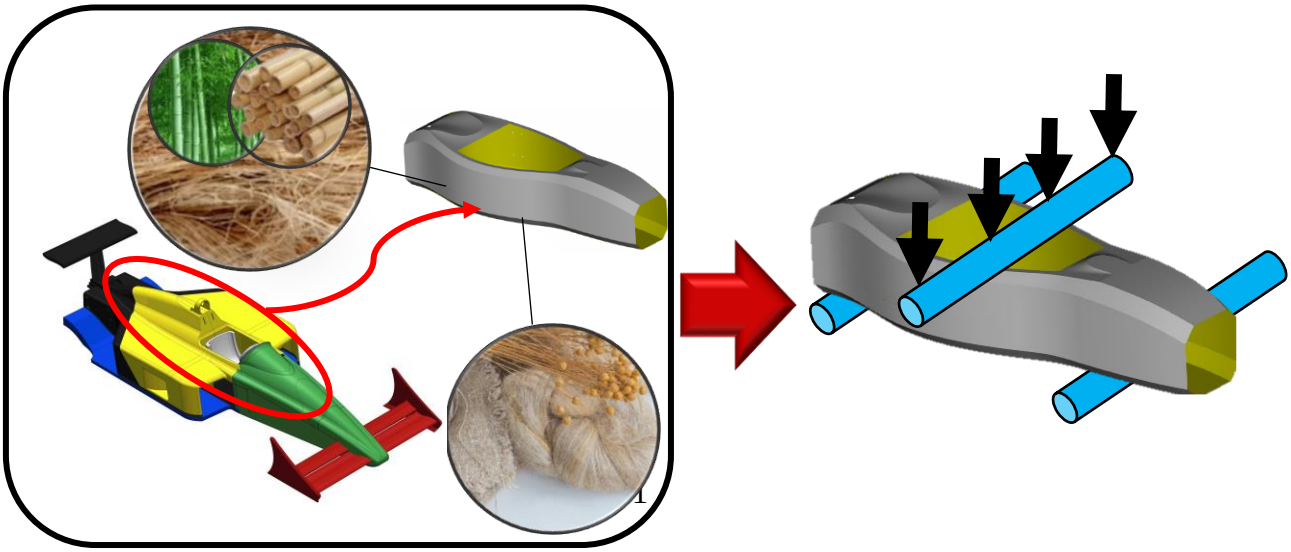

**Keywords:** Biocomposites, Micromechanics, Motorsport, Monocoque chassis, Elasto-visco-plasticity, Anisotropy, Effective properties, User- defined material, Finite Element Modelling.

# 1 Introduction

Circularity of materials is an important aspect of our sustainable development and transition to becoming a solid ecological society. Natural fibre-reinforced polymer composite materials have gained much interest due to the eco-environment requirements and the recyclability capabilities. Natural fibres are often classified based on their source. Among these fibres, those obtained from plants are extensively employed for various purposes and possess notable economic importance. In addition, natural fibres represent an alternative to glass and carbon fibres and can be used in bio or hybrid composites. Indeed, Mishra et al. [1] highlighted the advantages of natural fibres over traditional reinforcing fibres in terms of low cost, low density, mechanical properties, ease of separation, enhanced energy recovery, $CO_2$ sequestration and biodegradability. Moreover, they identified the role of fibre surface modification in the enhancement tensile and impact strengths as well as flexural strength of hybrid composites. Through microbond tests, Leduigou et al. [2] evaluated the interfacial shear strength of flax fibres reinforced polyamide studied the macroscale in-plane shear properties. Using experimental micrographs and analytical micromechanics models Zuccarello et al. [3] obtained an enhancement of mechanical matrix stiffness for agave long fibre biocomposites whereas for a given fibre treatment, the use of the more deformable PLA allows a better exploiting of the fibre properties, i.e. it leads always to more eco-friendly biocomposites with higher mechanical strength. A good review on natural fibres reinforced cellulosic composites can be found in works by John and Thomas [4].Thusly, biocomposites started to replace traditional plastics and composites. This can mean new kinds of vehicle body structures and designs for the transport system. In turn, this can mean new challenges in the construction so that safety standards are maintained and components continue to be protective for the occupants. Recently, motorsports have shown the industrial initiative to integrate biocomposites as structural components [5, 6, 7]. Simulation and modelling tools are beneficial in this development. However, due to biocomposites microstructure, current computer-aided engineering (CAE) analysis tools are insufficient to explore the wide range of possibilities during material selection and accurately predict components' behaviour. The present study is oriented towards establishing a predictive material model for portraying the behaviour of a biocomposite material encompassing multiple phases and its application using short bamboo and flax fibres-reinforced epoxy under different loading conditions.

## 1.1 Biocomposite in high-performance and structural applications

The literature contains several research studies involving high-performance characterisation and compression loading of biocomposite structures. For example, silk/epoxy composite tubes studied by Eshkoor et al. [8, 9, 10, 11], Ataollahi et al. [12], Ude et al. [13], flax/epoxy tubes studied by Yan and Chouw [14], Hu et al. [15], Yan et al. [16], flax/polymer by Tomlinson and Fam [17], jute/polyester by Mache et al. [18], jute/epoxy by Sivagurunathan et al. [19], hybrid jute/glass/epoxy by Albahash and Ansari [20], Attia et al. [21], hybrid kenaf/glass/epoxy by Supian et al. [22], Kumar et al. [23] and other materials such as ramie/epoxy by Ghoushji et al. [24], date palm leaf fibre/epoxy by Mahdi et al. [25] and kenaf fibre/wooden stick/epoxy by

Alkateb et al. [26]. As for the industrial sector, two companies YCOM (Italian motorsport engineering and lightweight composites firm) and Bcomp (a Swiss composites company), announced on October 2020 the successful crash test of an all-natural flax fibre (ampliTex™) front structure. In addition, other applications, such as the automotive chassis, assume paramount significance, as the weight and stiffness characteristics are intrinsically linked to the operational efficiency of the vehicle, the safety of its occupants and aerodynamic performance. Several EU-funded Horizon projects [27, 28] have researched the utilisation of biocomposite for chassis and structural components and the incorporation of high-performance biocomposites in the manufacture of automotive BiW [29]. According to McLaren, using natural fibre composites is the latest example of pioneering composite materials innovation and represents a step toward evolving sustainability [30].

However, the existing studies only focus on experimental work. Modelling and simulation studies to predict biocomposite materials' behaviour are very limited and underdeveloped. Among the existing finite element (FE) works, one can mention researches on crushing of cotton-fibres/polypropylene and silk/ epoxy tubes by Mahdi et al. [31] and Oshkovr et al. [32], respectively, with experiment-dependent material properties prior to creating and testing of a model.

## 1.2 Rate-dependent composite materials

Polymers-based matrix composites find interesting applications in technological domains due to their mechanical and thermal performances in terms of higher stiffness, strength, impact resistance, heat resistance, abrasion and wear resistance, and gas barrier. In the case of a polymer resin matrix, it can be noticed a rate dependent on the different stages of the deformation. Therefore, the stress–strain response depends on the strain rate. This behaviour results in rate-dependent (viscoplastic) constitutive models. Across the literature, several works have been developed to consider the elasto visco plasticity within micromechanics models. Using an affine homogenisation scheme, Pierard et al. [33] derive effective response random and homogeneous dispersion of spherical inclusions for different strain rate. Zhang and Yu [34] developed the variational asymptotic method for unit cell homogenisation VAMUCH and applied it to fibres reinforced composite. Marfia and Sacco [35] determine the effective nonlinear rate(in)dependent response of a periodic composite using a multiscale FE approach combining PieceWise Uniform Transformation Field Analysis (PWUTFA) homogenisation and the concept of the Unit Cell (UC) divided into subsets. Under three different radial and non-radial paths in strain space, Lahellec and Suquet [36] developed a rate-variational procedure (RVP) and full-field simulation (Fast Fourier Transform) to determine the effective behaviour of spherical inclusions reinforced elastic ideally plastic matrix and elastoplastic as well as rate dependent matrix. Kowalczyk-Gajewska–et al. [37] proposed an extension of elastic micromechanics to elastic-viscoplastic composites of the spatial distribution and morphology of particles through a cluster interaction model initially introduced by Molinari and El Mouden [38].

## 1.3 Anisotropy due to reinforcements

The spatial distribution and morphology of particles within the microstructure often lead to an anisotropic behaviour in the composite materials. The interaction between particles of a

composite material has been acknowledged as a precise approach for deriving the effective properties. Although, the morphological texture referring to the aspect ratio also play an important role in the response of the composite, the accuracy of predictive models resides their capabilities for accounting for the interaction between inclusions and their surrounding neighbourhood. This approach is the so-called multi-site modelling. In that context, Fassi-Fehri [39] identified some limitations and weaknesses of the modelling based on single inclusion, which fails to accurately predict the anisotropy induced by the morphological and topological textures of the composite. Earlier works dealing with the multi-site modelling, have been performed by Fassi-Ferhi et al. [40], Molinari and El Mouden [38], Broohm et al. [41]. Related research works dealing with the pairwise particle-interaction through a micromechanics formulation have been done for effective elastic properties by Ju and Chen [42, 43] and for randomly dispersed elastoplastic phases by Ju and Tseng [44], Ju and Sun [45] and Sun and Ju [46]. The multi-site modelling was used to derive the thermoelastic properties of anisotropic cubic composites by Kpobie et al. [47]. The framework of the multi-site modelling is used by Azoti et al. [48] to derive the macroscopic response of elastoplastic composites with ordered microstructures. And recently by Elmasry et al. [49] for the thermomechanical behaviour of graphene related composite materials.

## 1.4 Objectives of the work

As previously mentioned, the existing literature work of biocomposite material modelling and simulation is very limited and underdeveloped. The current study will focus on creating a predictive material model to depict the behaviour of multiphase bamboo/flax fibre-reinforced epoxy biocomposite. The created predictive model will depend only on available constituent material properties instead of requiring a priori experimentation to obtain the properties, as the case state in available finite element (FE) software. Afterwards, a comparison will be conducted between multi-site and one-site modelling approaches on the biocomposite behaviour, where the multi-site approach accounts for the interaction between inclusions and their surrounding neighbourhood; the one-site approach does not. Finally, the created model and algorithms will be implemented in a commercially available FE-solver (Abaqus®) as a user-defined materials UMAT. The bending load, deflection and energy absorption capabilities of a motorsport monocoque chassis structure will be analysed as an application to aid prospective designers and engineers. This analysis aims to provide insights into behavioural performance, facilitating judicious material and structural decision-making and obviating the necessity for extensive and resource-intensive physical testing.

## 1.5 Structure of the paper

The paper is organised as follows: Section 2 presents the analytical and FE modelling strategies and derives the micromechanics effective properties of a composite from the so-called multi-site modelling. It also provides details on the constitutive equations for the interaction's tensors and their numerical implementation. The nonlinear rate dependency of a phase is presented with the resulting regulated algorithmic tangent modulus. FE models and utilised boundary conditions are also illustrated. Section 3 presents the results and model validation by comparing the numerical predictions with respect to works from open literature. A multiscale FE simulation of the micromechanics is performed on a 3-phases bamboo/flax fibre-reinforced epoxy hybrid composite where micro parameters and state variables (volume fraction,

accumulated plastic strain, equivalent stress) are studied. Finally, a full motorsport monocoque chassis structure behaviour and deformability are analysed. Section 4 provides a discussion summarising the undertaken work and stressing some points. Section 5 concludes the paper.

# 2 Modelling methodology

## 2.1 Fundamentals of micromechanics

### *2.1.1 Constitutive equations*

For a macro homogeneous and micro heterogeneous material, considered for a representative volume element (RVE), the effective elastic constitutive law (Hooke law) is given such as:

$$\Sigma_{ij} = C_{ijkl}^{eff} E_{kl} \tag{1}$$

with $\Sigma_{ij}$, $E_{kl}$ representing respectively the components of the macroscopic stress and strain tensors. The stiffness tensor $C^{eff}$ stands for the effective fourth-order elastic tensor having the usual material symmetries. At each point $r$ inside the RVE, the local elastic constitutive behaviour is written such as:

$$\sigma_{ij}(r) = c_{ijkl}(r)\varepsilon_{kl}(r) \tag{2}$$

where $\sigma_{ij}$, $\varepsilon_{kl}$ and $c_{ijkl}$ represent respectively the components of the stress and strain tensors as well as the local stiffness tensor.

The scale transition is now introduced to make the relationship between the micro scale (local) and macro scale (global) elastic properties. It consists firstly in the localisation step by the global strain concentration tensor [50] $A$ such as:

$$\varepsilon_{ij}(r) = A_{ijkl}(r)E_{kl} \tag{3}$$

Then, the homogenisation step uses averaging techniques to approximate the macroscopic behaviour. Also, it is supposed that all the constituents in the RVE are perfectly bonded with respect to the matrix. Under these conditions, the following relationship between the macro scale and micro scale quantities yields [51]:

$$\sum_{ij} = \frac{1}{V}\int_V \sigma_{ij}(r)dV \tag{4}$$

$$E_{ij} = \frac{1}{V}\int_V \varepsilon_{ij}(r)dV \tag{5}$$

Substituting Eq. (3) in Eq. (2) and combining the result with Eq. (4), one can compare the resulting expression with Eq. (1). Then, the effective properties of the RVE are determined by:

$$C_{ijkl}^{eff} = \frac{1}{V}\int_V c_{ijmn}(r)A_{mnkl}(r)dV \tag{6}$$

Or in other terms

$$C^{eff} = c^0 + \sum_{I=1}^{N} f_I (c^I - c^0) : A^I \tag{7}$$

$c^I$, $A^I$, $f_I$ are respectively the elastic properties tensor, the concentration tensor and the volume fraction of the inclusion $I$ while $c^0$ stands for the elastic properties tensor of the matrix.

The strain concentration tensor $A$ represents the unknown of the problem and it contains all information about the microstructure. The general form of this tensor is given by an iterative procedure detailed in Elmasry et al. [52] such as:

$$\begin{cases} A(r) = a(r) : \langle a(r) \rangle^{-1} \\ \langle A(r) \rangle = \mathbf{I} \end{cases} \tag{8}$$

with $\mathbf{I}$ stating for the fourth identity tensor, whereas $a(r)$ defined by $\varepsilon(r) = a(r) : E^r$, represents a local strain concentration tensor with respect to an applied strain in a reference medium $E^r$. The symbol $\langle \bullet \rangle$ represents the averaging of the bracketed quantity. The strain concentration tensor $\boldsymbol{A}$ represents the unknown of the problem and it contains all information about the microstructure. Considering an RVE in which are $N$ ellipsoidal inhomogeneities and a surrounding matrix. The matrix phase is enumerated as 0, and the inhomogeneities phases range from 1 to $N$. The Eshelby's inclusion concept [53] is related to the elastic field in a medium disturbed by an inclusion that is embedded in an infinite matrix. In the particular case of ellipsoid inhomogeneity, and with the help of a set of imaginary cutting, straining and welding operations, Eshelby showed that under a uniform loading, the strain field inside it is uniform and may be expressed in terms of tabulated elliptic integrals. This fact enables the determination of effective properties of heterogeneous mediums considering the nature and the interaction between the inhomogeneities [49]:

$$a^I = \mathbf{I} - \sum_{J=0}^{N} T^{IJ} : \Delta c^J : a^J \tag{9}$$

$T^{IJ}$ represents the interaction tensor between inhomogeneities in the RVE. It is expressed such as:

$$T^{IJ} = \frac{1}{V^I} \int_{V^I} \int_{V^J} \Gamma(r - r') dV dV' \tag{10}$$

where Γ is the so-called modified Green tensor such as:

$$\Gamma_{mnij}(r - r') = -\frac{1}{2} \left\{ G_{mi,nj'}(r - r') + G_{ni,mj'}(r - r') \right\} \tag{11}$$

with $G_{mi}$ standing for the components of the Green's tensor.

The final expression of the strain concentration tensor is given by an iterative procedure [52]:

$$\begin{cases} (a^I)_0 = \mathbf{I} \\ (a^I)_{i+1} = (\mathbf{I} + T^{II} : \Delta c^I)^{-1} : \left( \mathbf{I} - \sum_{\substack{J=0 \\ J \neq I}}^{N} T^{IJ} : \Delta c^J : (a^J)_i \right) \\ I = 0,1,2,3, \ldots \ldots, N \end{cases} \tag{12}$$

When the Mori-Tanaka scheme is selected, the reference medium is assumed to be the matrix phase leading to $C^r = c^0$. Also, the average strain field inside the matrix is approximated by the strain within the reference medium leading to $a^o = \mathbf{I}$. Based on these assumptions, the effective properties according to the generalised Mori-Tanaka are given by:

$$C^{GMT} = \sum_{I=0}^{N} f_I c^I : A^I = (f_0 c^0 + \sum_{I=1}^{N} f_I c^I : a^I) : A^0 \tag{13}$$

with $A^0$denoting the global strain concentration tensor of the matrix. Its expression yields:

$$A^0 = a^0 : \langle a^I \rangle^{-1} = (f_0 \mathbf{I} + \sum_{I=1}^{N} f_I a^I)^{-1} \tag{14}$$

The derivation of above localisation procedures and the subsequent M-T effective properties depend on the computation of the interaction tensors $T^{II}$ and $T^{IJ}$expressed by Eq.(10).

### *2.1.2 Interaction tensor $T^{IJ}$ implementation*

Due to the presence of the Green's tensor which seems complex to calculate for an anisotropic medium, the evaluation of the interaction tensor for this medium remains difficult to calculate. A numeric method had been proposed for the problem of the ellipsoidal inhomogeneity by Fassi-Fehri [40].

#### *2.1.2.1 In one-site version: $T^{II}$*

Let us consider the Fourier transformation $\tilde{G}$ of the Green's function $G$:

$$\tilde{G}_{km}(\mathbb{k}) = \int_V G_{km}(r) e^{i\mathbb{k}_i r_i} dV \tag{15}$$

The inverse Fourier transformation is given by:

$$G_{km}(r) = \frac{1}{8\pi^3} \int_V \tilde{G}_{km}(\mathbb{k}) e^{-i\mathbb{k}_i r_i} dV \tag{16}$$

where $\mathbb{k}$ is the conjugate vector of $r$

The gradient $G_{km,lj}(r)$ of the inverse Fourier transformation is:

$$G_{km,lj}(r) = \frac{1}{8\pi^3} \int_V - \mathbb{K}_l \mathbb{K}_j \tilde{G}_{km}(\mathbb{K}) e^{-i\mathbb{K}_i r_i} dV \tag{17}$$

Also, the Fourier transformation $\tilde{\delta}$ of the Dirac function $\delta$ is given by:

$$\tilde{\delta}(\mathbb{K}) = \int_V \delta(r) e^{i\mathbb{K}_i r_i} dV = 1 \tag{18}$$

Its inverse Fourier transformation is:

$$\delta(r) = \frac{1}{8\pi^3}\int_V e^{-i\mathbb{k}_i r_i} dV \tag{19}$$

The Green's tensor can be verified such as:

$$C^r_{ijkl} G_{km,lj}(r) + \delta_{im}\delta(r) = 0 \tag{20}$$

Substituting Eq. (17) and Eq. (19) by their expressions in Eq.(20), one can show that:

$$C^r_{ijkl} \tilde{G}_{km}(\mathbb{k})\mathbb{k}_l\mathbb{k}_j = \delta_{im} \tag{21}$$

Substituting Eq.(11) in the expression of $T^{IJ}$ Eq.(10), one can note that

$$T^{II}_{klmj} = \frac{1}{2}\left(t^{II}_{klmj} + t^{II}_{lkmj}\right) \tag{22}$$

Where

$$t^{II}_{klmj} = -\frac{1}{V_I}\int_{V_I}\int_{V_I} G_{km,lj}(r - r')dV_I' dV_I \tag{23}$$

And substituting Eq. (17) in Eq.(23), the resultant expression of $t^{II}_{klmj}$is given by:

$$t^{II}_{klmj} = \frac{1}{8\pi^3 V_I}\int_{V_I}\int_{V_I}\int_{V_{\mathbb{k}}} \mathbb{k}_l\mathbb{k}_j \tilde{G}_{km}(\mathbb{k}) e^{i\mathbb{k}_i(r_i + r_i')} dV_{\mathbb{k}} dV_I dV_I' \tag{24}$$

In the case of an ellipsoidal inhomogeneity Fassi-Ferhi [40] had shown that the final expression of this interaction tensor is:

$$t^{II}_{klmj} = \frac{1}{4\pi}\int_{\theta=0}^{\pi}\int_{\varphi=0}^{2\pi} \chi_l\chi_j\kappa^2\tilde{G}_{km}(\mathbb{k})\sin\theta d\varphi d\theta \tag{25}$$

Where

$$\mathbb{k}_i = \kappa\chi_i, \qquad \kappa = |\mathbb{k}|, \qquad \chi = \begin{cases} \chi_1 = \sin\theta\cos\varphi \\ \chi_2 = \dfrac{a}{b}\sin\theta\sin\varphi \\ \chi_3 = \dfrac{a}{c}\cos\theta \end{cases} \tag{26}$$

And

$$\kappa^2\tilde{G}_{jk}(\mathbb{k}) = \left(C^r_{ijkl}\chi_i\chi_l\right)^{-1} \tag{27}$$

With $a$, $b$, $c$ the dimensions of the ellipsoidal.

#### 2.1.2.2 *In multi-site version:* $T^{IJ}$

The calculation of the interaction tensor $T^{IJ}$ is done in the inertia coordinate system of the inclusions $I$. In this coordinate system, let us denote:

- $(a_1, b_1, c_1)$ the dimension of the ellipsoidal inhomogeneity $I$ with origin $O_1$;
- $(a_2, b_2, c_2)$ the dimension of the ellipsoidal inhomogeneity $J$ with origin $O_2$;
- $\vec{R}^0$the vector such as $\vec{R}^0 = \overrightarrow{O_1O_2}$;
- $P_{ij}$the components of a transfer matrix from the orientation of inclusion $J$ with respect to the inclusion $I$ according to the angles of Euler.

According to Eq. (22), the expression of the interaction tensor $T^{IJ}$ is:

$$T^{IJ}_{klmj} = \frac{1}{2}\left(t^{IJ}_{klmj} + t^{IJ}_{lkmj}\right) \tag{28}$$

In the present case, the expression of the interaction tensor is given by [40, 54]:

$$t^{IJ}_{klmj} = \frac{9}{8\pi^3} V_J \int_{\theta=0}^{\pi} \int_{\varphi=0}^{2\pi} \chi_l \chi_j \kappa^2 \tilde{G}_{km}(\mathbb{k}) \sin(\theta) F(\theta, \varphi) d\varphi d\theta \tag{29}$$

The components of $\chi_i$ is given as:

$$\chi_i \text{ such as } \begin{cases} \chi_1 = \sin\theta\cos\varphi \\ \chi_2 = \sin\theta\sin\varphi \\ \chi_3 = \cos\theta \end{cases} \tag{30}$$

$$F(\theta, \varphi) = \frac{\pi}{48}\left\{\frac{f_1 + f_2 + f_3 + f_4}{(ab)^3}\right\} \tag{31}$$

$$\begin{cases} f_1 = |\alpha|[-\alpha^2 + 3(a+b)\alpha - 6ab] \\ f_2 = |\beta|[\beta^2 + 3(a-b)\beta - 6ab] \\ f_3 = |\gamma|[\gamma^2 - 3(a-b)\gamma - 6ab] \\ f_4 = |\delta|[-\delta^2 + 3(a+b)\delta - 6ab] \end{cases} \tag{32}$$

$$\begin{cases} \alpha = a + b - c \\ \beta = -a + b + c \\ \gamma = a - b + c \\ \delta = a + b + c \end{cases} \text{ in which } \begin{cases} a = (a_1^2\chi_1^2 + b_1^2\chi_2^2 + c_1^2\chi_3^2)^{\frac{1}{2}} \\ b = \left[a_2^2\left(\mathrm{P}_{1j}\chi_j\right)^2 + b_2^2\left(\mathrm{P}_{2j}\chi_j\right)^2 + c_2^2\left(\mathrm{P}_{3j}\chi_j\right)^2\right]^{\frac{1}{2}} \\ c = \chi_1 R_1^0 + \chi_2 R_2^0 + \chi_3 R_3^0 \end{cases} \tag{33}$$

293 *2.1.2.3 Implementation steps*

294 The computation of $T^{II}$ and $T^{IJ}$ leads to the calculation of double integrals Eq. (25) and (29)
295 with trigonometric variables$(\theta, \varphi)$. The Fourier series transformation used in the case of
296 periodic functions allows a numerical approximation of these integrals such as [55]:

$$\begin{cases} \int_{\theta=0}^{\pi} \int_{\varphi=0}^{2\pi} f(\theta,\varphi) d\varphi d\theta = \dfrac{2\pi^2}{NM} \sum_{i=1}^{N} \sum_{j=1}^{M} f\left(\theta_i, \varphi_j\right) \\ \theta_i = \dfrac{\pi}{N}(i-1), \qquad \varphi_j = \dfrac{2\pi}{M}(j-1) \end{cases} \tag{34}$$

297

298 In Eq. (34), $M$ and $N$ are Gauss integration points in the variables $(\theta, \varphi)$ direction. Following
299 steps allow the implementation of the interaction tensors

300 - **in one site version:**

301 - Compute vector $\boldsymbol{\chi}$ from Eq. (26);
302 - Compute tensor $\kappa^2 \tilde{G}_{jk}(\mathbb{k})$ from Eq.(27);
303 - Compute integral $t^{II}$ from Eq. (25) by using transformation in Eq. (34);
304 - And finally compute interaction tensor $T^{II}$ from Eq. (22).

305 - **in multi-site version**:

306 - Compute vector $\boldsymbol{\chi}$ from Eq. (30) and function $F(\theta, \varphi)$ from Eq. (31) using
307 Eqs.(32),(33);
308 - Compute $\kappa^2 \tilde{G}_{km}(\mathbb{k})$ from Eq.(27), and compute $t^{IJ}$ from Eq.(29);
309 - And finally, compute $T^{IJ}$ from Eq.(28).

310

311 ***2.1.3 Rate dependent Viscoplastic behaviour***

312 The additive decomposition of the total strain into an elastic and viscoplastic parts and its
313 application on the Hooke law give:

$$\begin{cases} \boldsymbol{\varepsilon} = \boldsymbol{\varepsilon}^e + \boldsymbol{\varepsilon}^{vp} \\ \boldsymbol{\sigma} = \boldsymbol{C}^{el} : \boldsymbol{\varepsilon}^e = \boldsymbol{C}^{el} : (\boldsymbol{\varepsilon} - \boldsymbol{\varepsilon}^{vp}) \\ \boldsymbol{C}^{el} = 2G\left(\mathbf{I} - \dfrac{1}{3}\mathbf{1} \otimes \mathbf{1}\right) + K\mathbf{1} \otimes \mathbf{1} \end{cases} \tag{35}$$

314

315 With $\boldsymbol{G}$ and $\boldsymbol{K}$ denoting the shear and bulk modulus respectively.
316 Using the von Mises plasticity with an isotropic hardening to represent the viscoplastic effects
317 , the yield criterion is given such as [56] :

$$\begin{cases} f\left(\sigma_{eq}, p, \dot{\varepsilon}\right) = \sigma_{eq} - \left[\sigma_y(\dot{\varepsilon}) + R(p)\right] \\ \sigma_{eq} = \sqrt{\dfrac{3}{2}\boldsymbol{s} : \boldsymbol{s}} \\ \boldsymbol{s} = \boldsymbol{\sigma} - \dfrac{1}{3}(\mathrm{tr}\,\sigma)\mathbf{1} \end{cases} \tag{36}$$

318

where $\boldsymbol{\sigma_{eq}}$is the equivalent stress, $\boldsymbol{\sigma_y}$ is the yield stress indicating the elasticity limit (which may depend on the strain rate ) and $\boldsymbol{R(p)}$ is the hardening function. The accumulative viscoplastic strain $\boldsymbol{p}$ is an internal variable that preserves the history of deformation. It is given such as:

$$\begin{cases} p(t) = \int_0^t \dot{p}(\tau) d\tau \\ \dot{p} = \sqrt{\frac{2}{3} \dot{\boldsymbol{\varepsilon}}^{vp} : \dot{\boldsymbol{\varepsilon}}^{vp}} \end{cases} \tag{37}$$

The viscoplastic strain rate $\dot{\boldsymbol{\varepsilon}}^{\boldsymbol{vp}}$ follows a plastic flow rule given by:

$$\dot{\boldsymbol{\varepsilon}}^{vp} = \dot{p} \frac{\partial f}{\partial \boldsymbol{\sigma}} = \dot{p} \boldsymbol{N} \tag{38}$$

where the tensor $\boldsymbol{N}$ is written such as:

$$\begin{cases} \boldsymbol{N} = \frac{3}{2} \frac{\boldsymbol{s}}{\sigma_{eq}} \\ \boldsymbol{N} : \boldsymbol{N} = \frac{3}{2} \end{cases} \tag{39}$$

and the plastic multiplier $\dot{\boldsymbol{p}}$ is defined by a viscoplastic function $\mathbf{g_v}$ such as:

$$\begin{cases} \dot{p} = 0 & \text{if } f \leq 0 \\ \dot{p} = \mathrm{g}_v(\sigma_{eq}, p, \dot{\varepsilon}) & \text{if } f > 0 \end{cases} \tag{40}$$

Substituting Eq. (40) into Eq. (38) leads to :

$$\dot{\boldsymbol{\varepsilon}}^{vp} = \mathrm{g}_v(\sigma_{eq}, p, \dot{\varepsilon}) \frac{\partial f}{\partial \boldsymbol{\sigma}} \tag{41}$$

The implicit backward Euler integration scheme can be introduced for the Viscoplastic strain by:

$$\begin{cases} \Delta \boldsymbol{\varepsilon}^{vp} = \dot{\boldsymbol{\varepsilon}}^{vp} \Delta t \\ \Delta p = \dot{p} \Delta t \end{cases} \tag{42}$$

with $\Delta \bullet = (\bullet|_{t_{n+1}} - \bullet|_{t_n})$ stands for a discretisation in time interval.

Applying Eq. (42) on Eq. (38), gives:

$$\Delta \boldsymbol{\varepsilon}^{vp} = \boldsymbol{N} \Delta p \tag{43}$$

The use of the radial return mapping algorithm [57] in elasto-viscoplastic on Eq. (35) gives for the updated stress:

$$\begin{cases} \boldsymbol{\sigma} = \boldsymbol{\sigma}^{trial} - 2G \Delta \boldsymbol{\varepsilon}^{vp} \\ \boldsymbol{s} = \boldsymbol{s}^{trial} - 2G \Delta \boldsymbol{\varepsilon}^{vp} \end{cases} \tag{44}$$

Combining Eq. (39)-a and Eq. (43) and substituting the recasted expression into Eq. (44)-b lead to:

$$3G\Delta p + R(p) + \sigma_Y - \sigma_{eq}^{trial} = 0 \tag{45}$$

Eq. (40) -b can be rewritten using the implicit backward Euler integration scheme such as:

$$\Delta p - \mathrm{g}_v(\sigma_{eq}, p, \dot{\varepsilon})\Delta t = 0 \tag{46}$$

The Eq. (45) and Eq. (46) give a system of equations with unknow state variables $(p, \sigma_{eq})$:

$$\begin{cases} 3G\Delta p + R(p) + \sigma_Y - \sigma_{eq}^{trial} = 0 \\ \Delta p - \mathrm{g}_v(\sigma_{eq}, p, \dot{\varepsilon})\Delta t = 0 \end{cases} \tag{47}$$

The above system is resolved numerically using the Newton method. Considering finite stress and strain increments, an algorithmic tangent operator $\boldsymbol{C}^{\mathrm{alg}}$ is derived from a linearisation of the constitutive equations over time $t_{n+1}$ such as:

$$\delta\boldsymbol{\sigma}(t_{n+1}) = \boldsymbol{C}^{\mathrm{alg}} : \delta\boldsymbol{\varepsilon}(t_{n+1}) \tag{48}$$

where $\delta$ means a total variation at $t_{n+1}$. The expression of the algorithmic tangent operator is given by [54]:

$$\begin{cases} \boldsymbol{C}^{\mathrm{alg}} = \boldsymbol{E}^{el} - \dfrac{(2G)^2}{h_v}\boldsymbol{N}\otimes\boldsymbol{N} - (2G)^2\dfrac{\sigma_{eq}\Delta p}{\sigma_{eq}+3G\Delta p}\dfrac{\partial \boldsymbol{N}}{\partial\sigma} \\ \boldsymbol{E}^{el} = 2G\boldsymbol{I}^{dev} + 3K\boldsymbol{I}^{vol} \\ h_v = \dfrac{1}{(\Delta t)\mathrm{g}_{,\sigma}} + 3G - \dfrac{\mathrm{g}_{,p}}{\mathrm{g}_{,\sigma}} \end{cases} \tag{49}$$

considering viscoplastic function $\mathbf{g_v}$ with two parameters: the viscoplastic module ($\boldsymbol{\kappa}[\mathbf{1/s}]$) and the exponent ($\boldsymbol{m}$) that appear as follows:

$$\mathrm{g}_{v(\sigma_{eq},p)} = \begin{cases} \kappa\left(\dfrac{f}{\sigma_y + R(p)}\right)^m & \text{if } f > 0 \\ 0 & \text{else} \end{cases} \tag{50}$$

$$\begin{cases} \mathrm{g}_{,\sigma} = m\dfrac{\mathrm{g}_v}{f} \\ \mathrm{g}_{,p} = -m\mathrm{g}_v\dfrac{dR}{dp}\left(\dfrac{1}{f} + \dfrac{1}{\sigma_y + R(p)}\right) \\ h_v = \dfrac{f}{m\mathrm{g}_v(\Delta t)} + 3G + \dfrac{dR}{dp}\dfrac{\sigma_{eq}}{\sigma_y + R(p)} \end{cases} \tag{51}$$

It can be shown that $\boldsymbol{h_v} \to \infty$ for very small increments of time i.e. when $\boldsymbol{\Delta t} \to \mathbf{0}$, a fact which is unacceptable (because $\boldsymbol{C^{alg}}$ then approaches $\boldsymbol{E^{el}}$ although $\dot{\boldsymbol{\varepsilon}}^{\boldsymbol{v_p}} \neq \mathbf{0}$). To solve the problem, Doghri et al. [58] have developed a method of regulation in elasto-viscoplastic from a 1D

analytical tangent expression valid for the simplest case (uniaxial- monotonous tension, constant deformation velocity, linear isotropic hardening and linear viscous stress).

$$\begin{cases} \boldsymbol{C}^{reg}(t_{n+1}) = \boldsymbol{C}^{ep}(t_{n+1}) + [\boldsymbol{C}^{reg}(t_n) - \boldsymbol{C}^{ep}(t_{n+1})]\exp\left(-\dfrac{h_{ep}}{h_v - h_{ep}}\right) \\ \boldsymbol{C}^{ep} = \boldsymbol{E}^{el} - \dfrac{(2G)^2}{h_{ep}}\boldsymbol{N} \otimes \boldsymbol{N} \\ h_{ep} = 3G - \dfrac{\mathrm{g}_{,p}}{\mathrm{g}_{,\sigma}} \end{cases} \tag{52}$$

The algorithmic tangent operator obtained from Eq. (52) will serve as properties of the nonlinear phase in the homogenisation process obtained by the Eq. (13)-(14). From this model, validations and numerical applications will be carried out on data from the literature and composites with particles and plant fibres.

### *2.1.4 Computing algorithm*

For a time $[t_n, t_{n+1}]$ increment, the input variables of the problem are: the macro strain $\mathbf{E}_n$ at $t_n$ and the macro strain increment $\Delta\mathbf{E}$ such as $\mathbf{E}_{n+1} = \mathbf{E}_n + \Delta\mathbf{E}$. The output variable is the macro stress such as $\boldsymbol{\Sigma}_{n+1} = \boldsymbol{\Sigma}_n + \Delta\boldsymbol{\Sigma}$. The general computational process outlined below was used to generate the final 2- and 3-phases composite response.

**Step1.**The starting input of the algorithms, as shown in Figure 1 and Figure 2, is the analytically applied strain increments. The strain increment $\Delta\mathbf{E}$ is first applied to the 3-phases composite (Figure 2) to generate strain of phase 1 inclusion, and then a partition of $\Delta\mathbf{E}$ namely $\boldsymbol{\Delta\varepsilon}$ is then performed between the remaining inclusion (or phase 2) and the matrix (Figure 1).

**Step2.** The algorithmic tangent operator of each phase is computed using Eq.(52). Due to its robustness, the generalised mid-point rule (Eq. (53)) is applied to the algorithmic tangent operator to derive the global strain concentration tensor $\boldsymbol{A}^I$.

$$\left[\boldsymbol{C}_0^{reg}\right]_{n+\alpha} = (1-\xi)\left[\boldsymbol{C}_0^{reg}\right]_n + \xi\left[\boldsymbol{C}_0^{reg}\right]_{n+1}, \qquad \xi \in [0,1] \tag{53}$$

**Step3.** After a convergence check is conducted, if it is determined that the iterative process has indeed converged, the effective properties of the composite system are calculated utilising Eq.(13). On the other hand, if the convergence check indicates that convergence has not been attained, it signifies that the solution has not yet reached a stable state. In such cases, the algorithm reverts back to **Step1**, restarting the iterative procedure to further refine the solution until convergence is eventually achieved.

**Step4.** At the end of **Step3** the output of the algorithm is tensor $\boldsymbol{C}^{GMT}$ and the stress increment $\Delta\sum$ that encapsulates the multiscale modelling of the 3-phases composite and contributions of these phases, providing valuable insights into the overall behaviour and response of the composite under varying conditions.

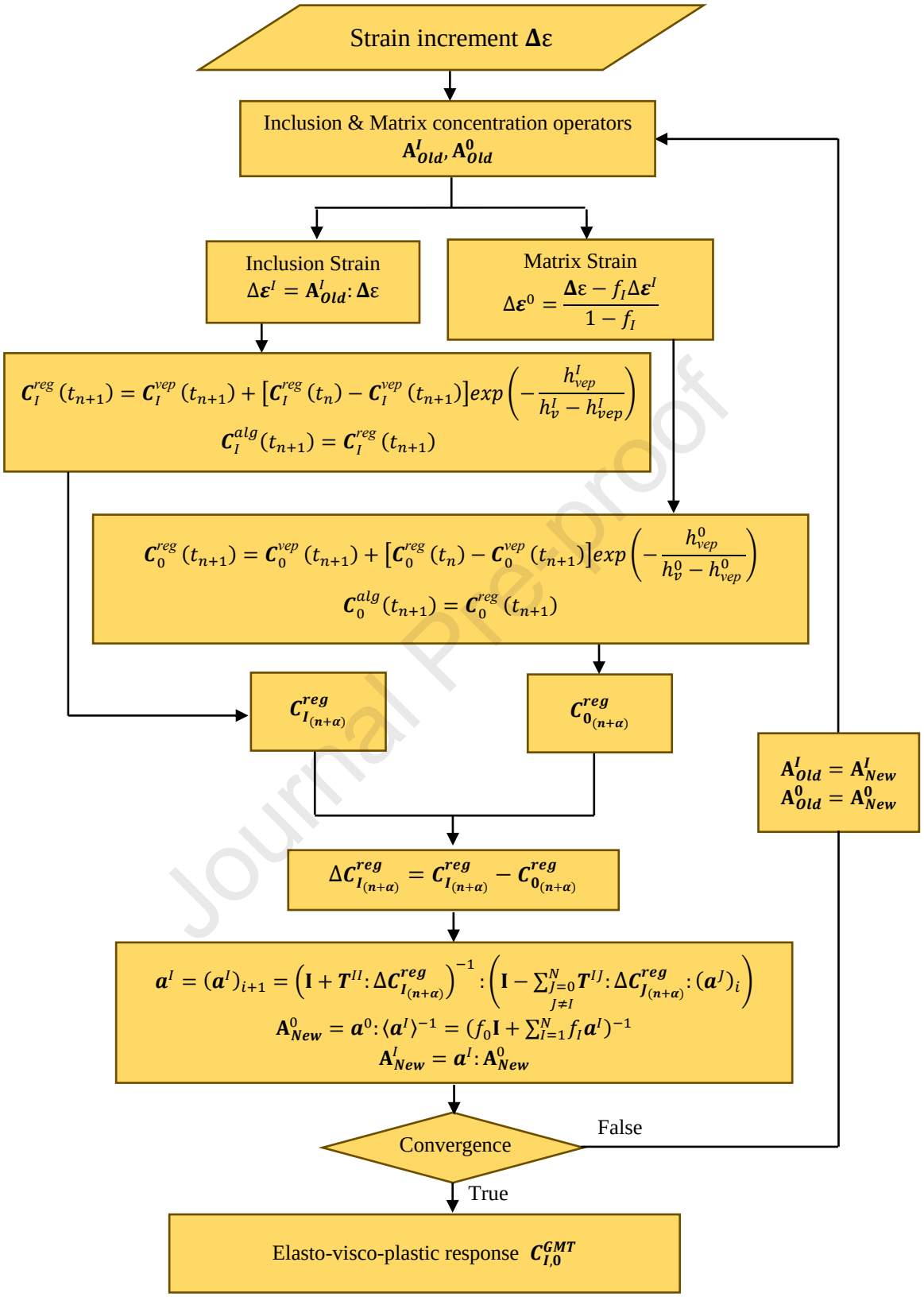


***Figure 1*** *Algorithm for analytical solving the nonlinear response of the 2-phases composite.*

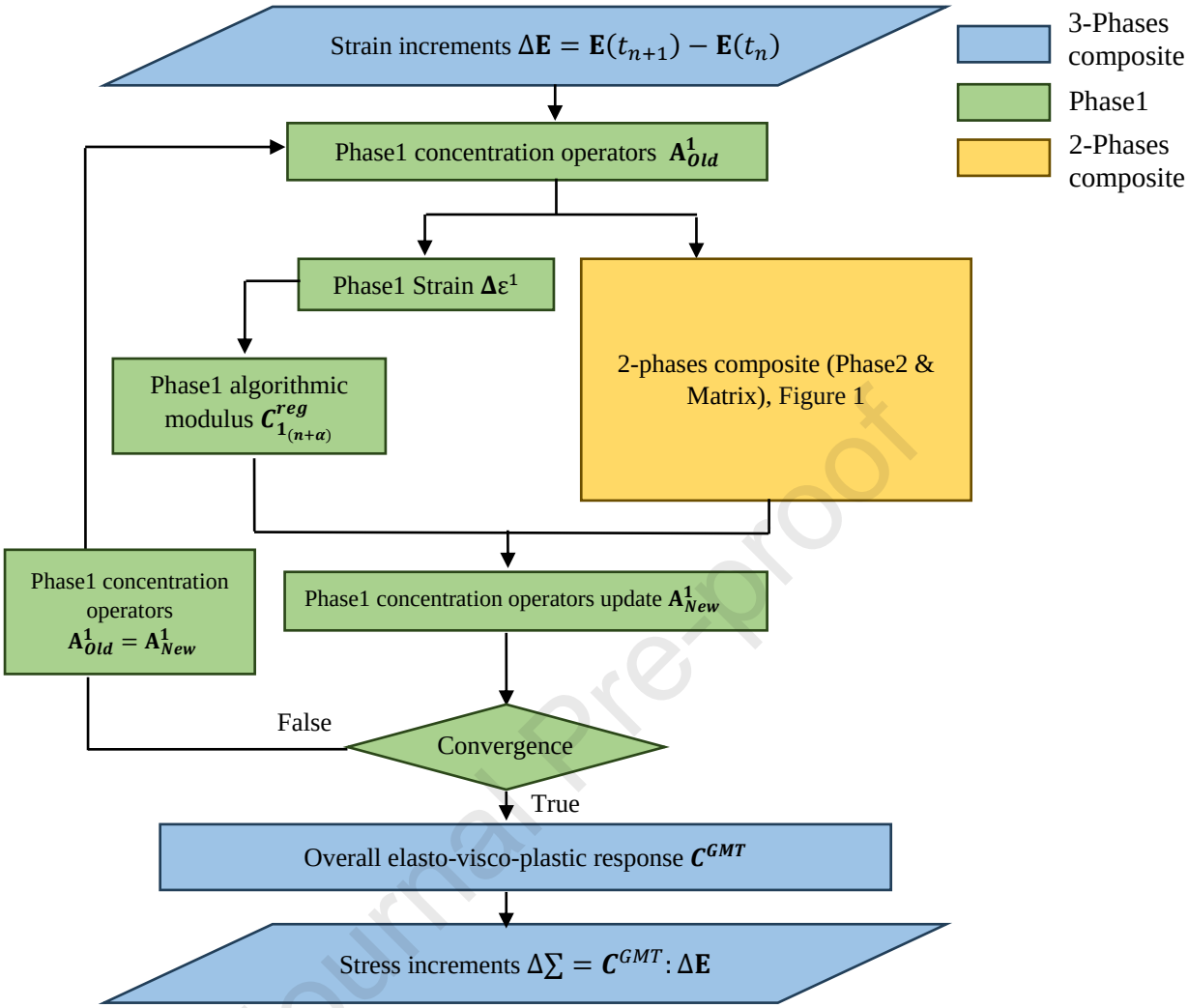


***Figure 2*** *Algorithm for analytical solving the nonlinear response of the 3-phases composite.*

## 2.2 Finite element (FE) modelling

For the numerical finite element (FE) modelling, Abaqus Software version (2022) is employed. Compiling process of user-defined materials was made using the model Intel® Fortran Compiler Classic for applications running on Intel(R) 64, version 2021.1.1 in combination with Microsoft Visual Studio® 2019. Abaqus/CAE 2022 is employed to construct the input files and view the results. The prevailing programming language for Abaqus UMAT is Fortran 77 but may also support Fortran 90. Construction of curves and plotting of equations were executed using Python 3.7.6 coding. SOLIDWORKS® 2021 was utilised to generate the CAD files. The meshed models were generated in BETA CAE Systems ANSA® v24.0.0, the mesh generator used with Abaqus.

### *2.2.1 Tensile testing*

A model of a tensile specimen is created in Abaqus with geometry according to the recommendations of ASTM-E8M [59], which are also comparable to tensile test specimen dimensions for reinforced composites conforming to the dimensions of the Type I specimen of ASTM D638 [60] and also comparable to ASTM D3039/D3039M [61].

Within Abaqus/Standard, one end of the specimen is fixed for two through-thickness 3D hexahedral elements of type C3D8I, and displacement boundary conditions are applied to the other end.

### *2.2.2 3-Point bending*

A model of a 3-point bending panel is also created within Abaqus/Standard according to the recommendations of ASTM-D7264M [62]. The panel rests on two supports and is loaded by means of a loading nose midway between the supports. Loading conducted by a prescribed vertical displacement has been introduced in the subsequent loading step of the analyses. The displacement has been introduced through the upper loading nose along the whole width of the panel.

### *2.2.3 Motorsport vehicle monocoque chassis structure*

A full motorsport monocoque chassis structure dimensions are depicted in Figure 3, while the FE model and boundary conditions employed for rigidity testing are in Figure 4. Abaqus/Standard with Hexahedral elements of type C3D8 were used. The load is applied to the middle section of the structure via a loading nose, allowing displacement to be only possible in one linear direction (y-direction) while the chassis rests on two supports.

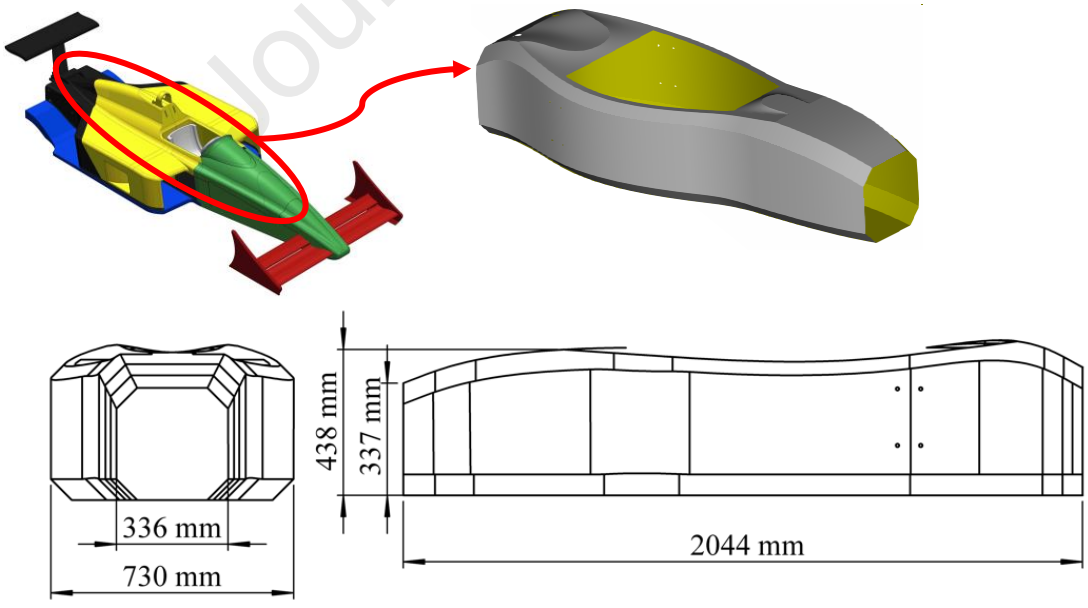


***Figure 3*** *Motorsport vehicle monocoque chassis structure dimensions.*

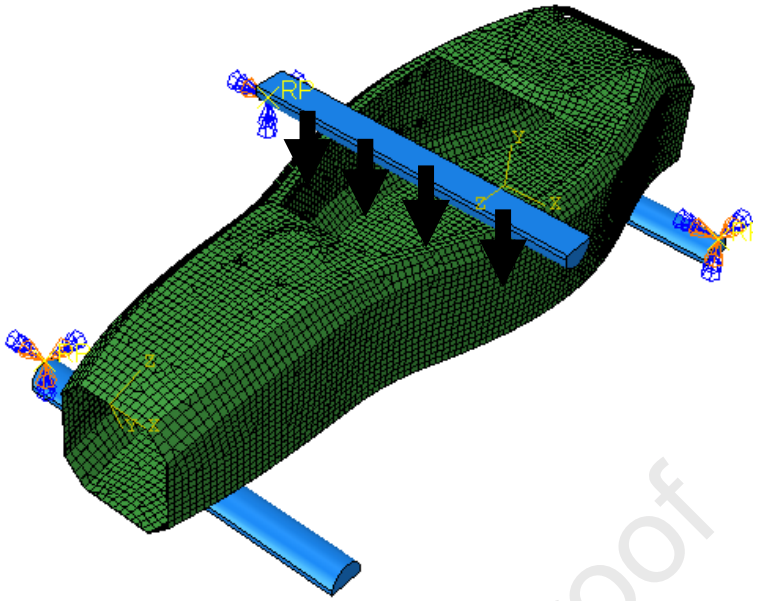


***Figure 4*** *Boundary conditions applied to motorsport vehicle monocoque chassis structure.*

### *2.2.4 Finite element analysis algorithm*

The algorithm illustrated in Figure 5 was employed to conduct finite element analysis and comprehend the overall behaviour of composite material consisting of both 2-phases and 3-phases components. The computational procedure is as follows:

**Step1.**The starting inputs of the algorithm are the numerically generated strain increments and time steps from the FE Abaqus code, along with material constants and history parameters (stored in state variables) would then be sent to the user-defined material code (UMAT).

**Step2.** The strain increment is divided into two distinct components: the first component corresponds to the strain induced by the inclusion of phase 1, while the second component represents a partitioned portion that is allocated to both the remaining phases, i.e. phase 2 and the matrix.

**Step2.** The algorithmic tangent operator of each phase is computed using Eq.(52) in conjunction with the generalised mid-point rule, as defined by Eq. (53), to derive the global strain concentration tensor.

**Step3.** After a convergence checking, if converged, the effective properties are obtained using Eq.(13) and the state variables are updated to correspond to the current time step. In contrast, if not converged **Step2** is repeated, restarting the process in order to iteratively refine the solution until convergence is eventually reached.

**Step4.** At the end of **Step3**, the failure condition is checked. In the event that the condition evaluates to false, the process of **Step1** is reiterated. Conversely, if the condition is deemed true, the element in question is subsequently removed or deleted.

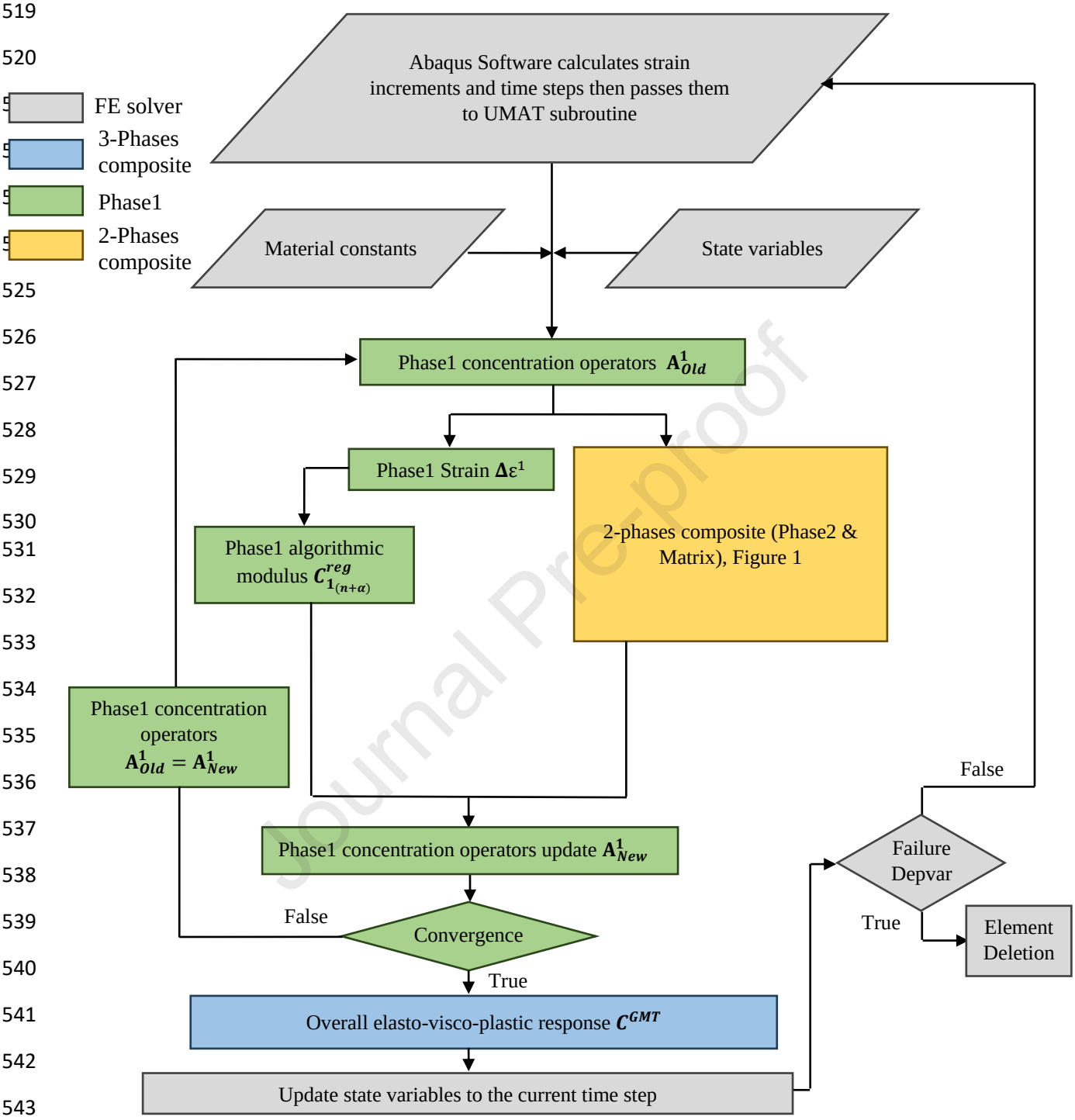


***Figure 5*** *Finite element analysis flow chart of 3 phases composite elasto-visco-plastic behaviour.*

# 3 Results

## 3.1 Models performance assessment

An extensive evaluation is conducted by comparing the performance of the proposed approaches against various existing approaches to ensure their robustness and reliability. Thus, valuable insights are gained into how well the current models execute, validate their effectiveness in a broader context and enable making informed judgments about the strengths and weaknesses of the approach, ultimately leading to a more thorough understanding of their capabilities and potential for different applications.

### *3.1.1 Mono-disperse spherical inclusions reinforced matrix composites*

This composite has been studied by Lahellec and Suquet [36] in the framework of Rate Variational Procedure (RVP) modelling. It consists of spherical inclusions with a volume fraction $f_I = 0.17$ randomly embedded in a surrounding matrix phase. The inclusions are considered elastic and isotropic while a rate-(in)dependent behaviour is retained for the matrix with an isotropic hardening function such as $R(p) = kp^n$. The material properties for such a composite are presented in Table 1.

***Table 1*** *Material properties [36].*

| **Matrix phase** | | | | | | | **Inclusions** | |
|---|---|---|---|---|---|---|---|---|
| **Shear modulus $G$ (GPa)** | **Bulk modulus $K$ (GPa)** | **Hardening parameters** | | **Visco plastic parameters** | | **Yield stress$\sigma_Y$ (MPa)** | **Shear modulus $G$ (GPa)** | **Bulk modulus $K$ (GPa)** |
| | | $k$ **(MPa)** | $n$ | $\kappa(s^{-1})$ | $m$ | | | |
| 3 | 10 | - | - | 1 | 1/0.3 | 100 | 6 | 20 |

- Case of elasto-ideally plastic matrix composite under a tension-torsion loading

The applied time-dependent macro stain increment $\Delta\mathbf{E}(t)$ on the RVE results in a combination of tension and torsion given by:

$$\Delta\mathbf{E}(t) = \Delta E_{33}(t)\left[-\frac{1}{2}\mathbf{e}_1 \otimes \mathbf{e}_1 - \frac{1}{2}\mathbf{e}_2 \otimes \mathbf{e}_2 + \mathbf{e}_3 \otimes \mathbf{e}_3\right] + \Delta E_{13}(t)[\mathbf{e}_1 \otimes \mathbf{e}_3 + \mathbf{e}_3 \otimes \mathbf{e}_1 + \mathbf{e}_2 \otimes \mathbf{e}_3 + \mathbf{e}_3 \otimes \mathbf{e}_2] \quad (54)$$

where the analytical expressions of the axial $\Delta E_{33}(t)$ and shear $\Delta E_{13}(t)$ strain components can be deduced from Fig. 2b of works by Lahellec and Suquet [36], as shown in Figure 6.

Figure 7 depicts inclusion and matrix phase materials' responses and compares current approaches (one-site and multi-site), and Fig.4 Lahellec and Suquet [36] RVP and FFT models considering elastic ideally-plastic matrix. In Figure 7 (a) the prescribed path in strain space is illustrated. The corresponding path in stress space is presented in Figure 7 (b), revealing that the current models closely align with and lie between the RVP and FFT models. Moreover, on average, similar behaviour is observed with macroscopic axial stress, as shown in Figure 7 (c) and with macroscopic shear stress in Figure 7 (d).

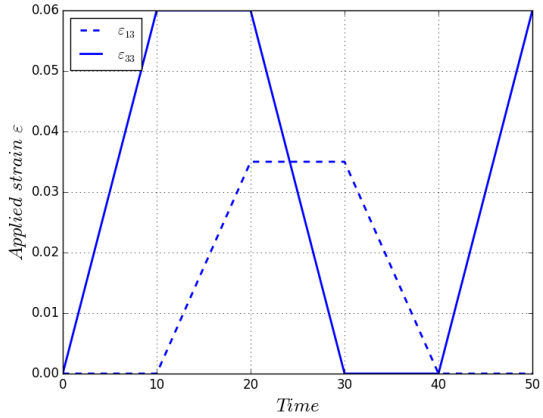


579

580 ***Figure 6*** *Loading history $\Delta E_{33}(t)$ macroscopic axial strain, $\Delta E_{33}(t)$ macroscopic shear*
581 *strain according to Fig. 2b Lahellec and Suquet [36].*

582

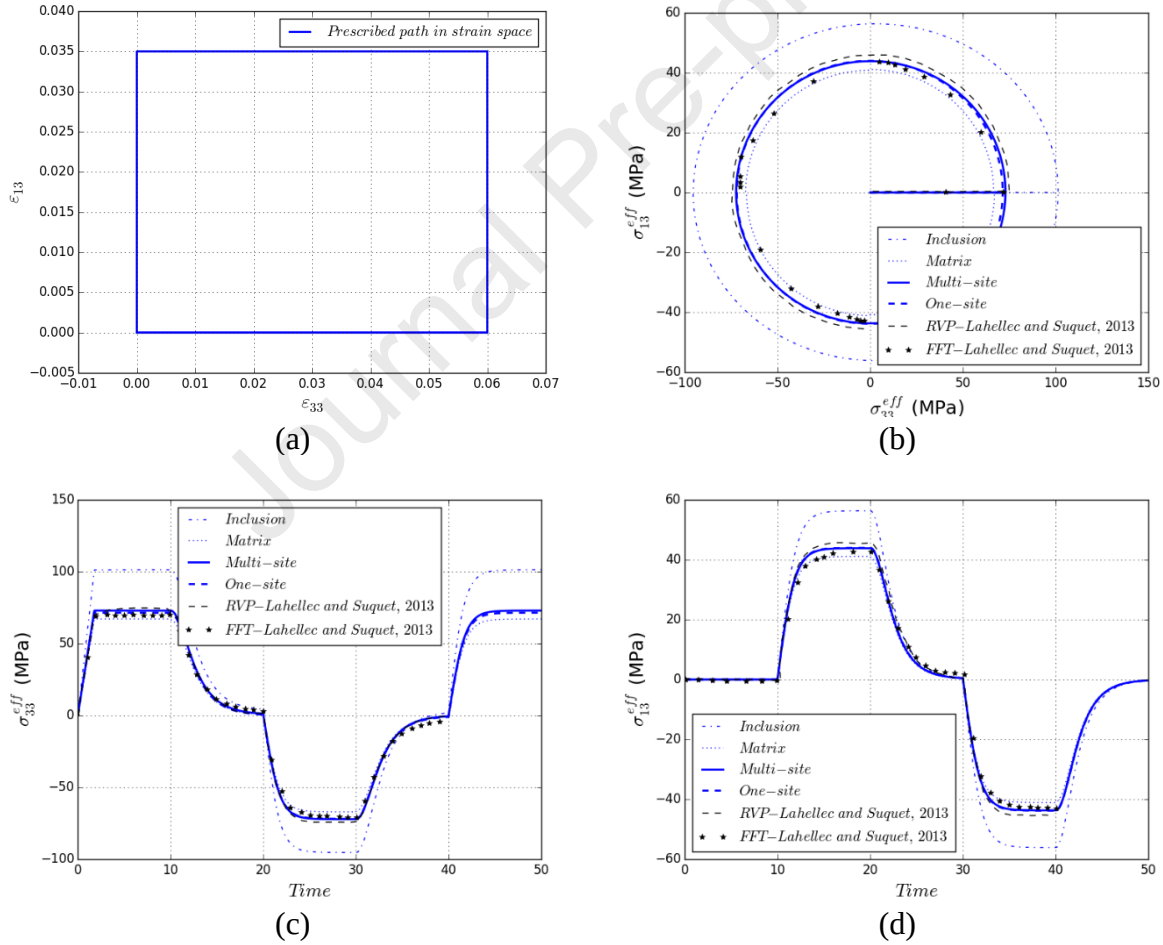


583

584 ***Figure 7*** *Elastic ideally-plastic matrix. Comparison between inclusion, matrix, one-site,*
585 *multi-site, and Fig.4 Lahellec and Suquet [36] RVP and FFT models :* (a) *Prescribed path in*
586 *strain space.* (b) *Resulting path in stress space.* (c) *Macroscopic axial stress.* (d) *Macroscopic*
587 *shear stress.*

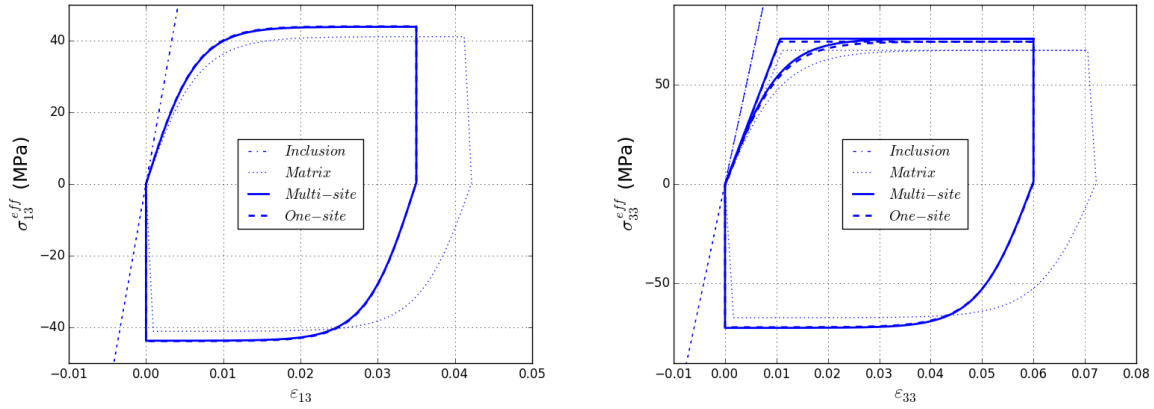


(a) (b)

588

589 ***Figure 8*** *Elastic ideally-plastic matrix. Radial loading–unloading of inclusion, matrix, one-*
590 *site, multi-site :* (a) *Macroscopic shear stress and* (b) *Macroscopic stress in the axial*
591 *direction as in Fig.3a Lahellec and Suquet [36].*

592 Figure 8 presents a comparison between the one-site and multi-site approaches under radial
593 loading–unloading. In Figure 8 (a), both methods exhibit the same shear stress response.
594 However, for the stress in the axial direction in Figure 8 (b), there is a slight discrepancy
595 between the models' responses, where they seem to shift. Overall, when considering the elasto-
596 ideally plastic matrix composite subjected to tension-torsion loading, there is a strong
597 agreement between the findings of Lahellec and Suquet [36] and the proposed approaches.
598 Additionally, no significant engineering differences were observed between the proposed
599 approaches.

600 ▪ Case of elasto-visco plastic matrix composite under uniaxial loading

601 The model's predictions have also been tested against Lahellec and Suquet's [36] results of
602 monotonic loading tests conducted at various strain rates, as shown in Figure 9. The model
603 effectively reproduces the overall stress levels with rate sensitivity. However, the current
604 approaches produce lower strength. In addition, the difference in stiffness is not observable at
605 a higher strain rate but decreasing the strain rate makes the difference in stiffness more
606 observable.

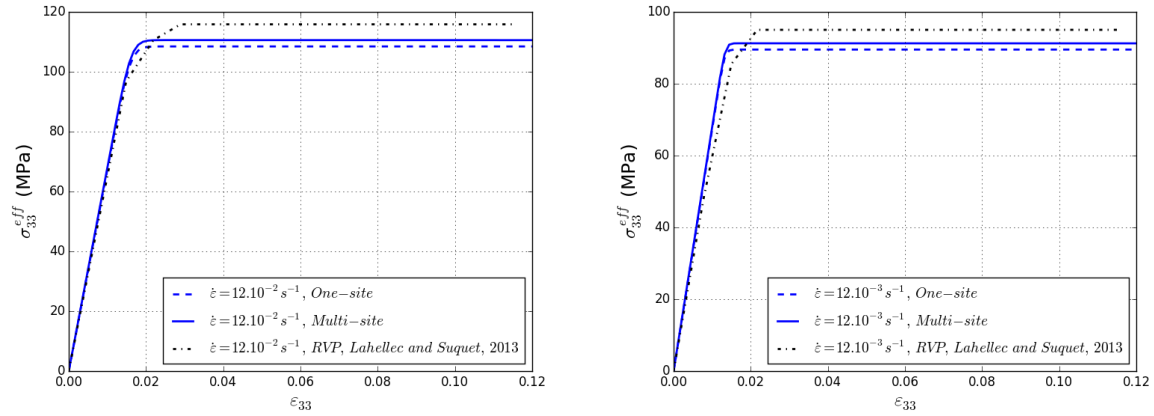


(a) (b)

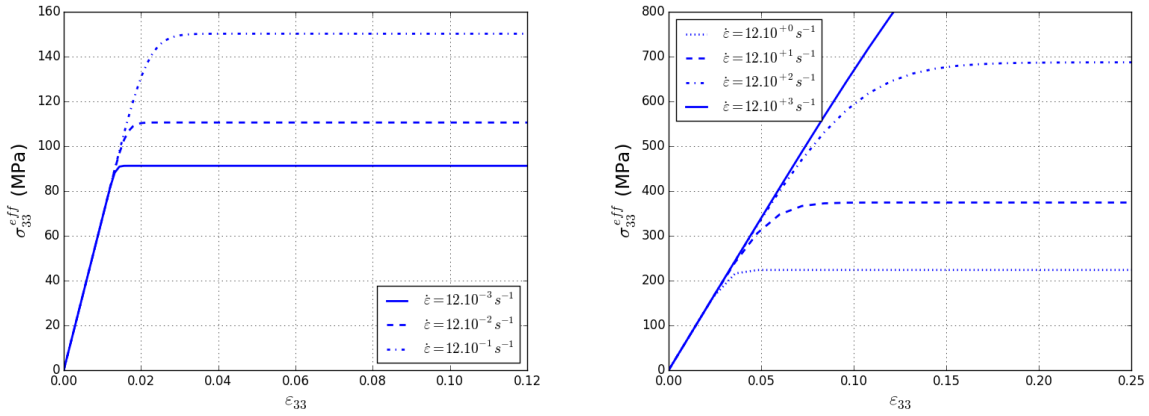


(c) (d)

***Figure 9*** *Rate-dependent matrix monotonic loading:*(a) *Comparison between one-site, multi-site, and Fig.9 Lahellec and Suquet [36] RVP model, at higher strain-rate,* (b) *at lower strain-rate, (c) and (d) at different strain-rates.*

- Case of elasto-visco plastic matrix composite under cyclic loading

The predictions of the model are compared with Lahellec and Suquet's [36] results in Figure 10 under cyclic loading. Once more, it is evident that the current model's correspondence with the reference results pertaining to the composite's overall response is deemed reasonably commendable. This implies that the predictions generated by the current model are closely aligned with the established reference data, signifying a favourable level of accuracy and reliability in assessing the composite material's overall behaviour and properties. Such a validation further reinforces the model's credibility and underscores its capability to yield meaningful and dependable outcomes in composite material analysis.

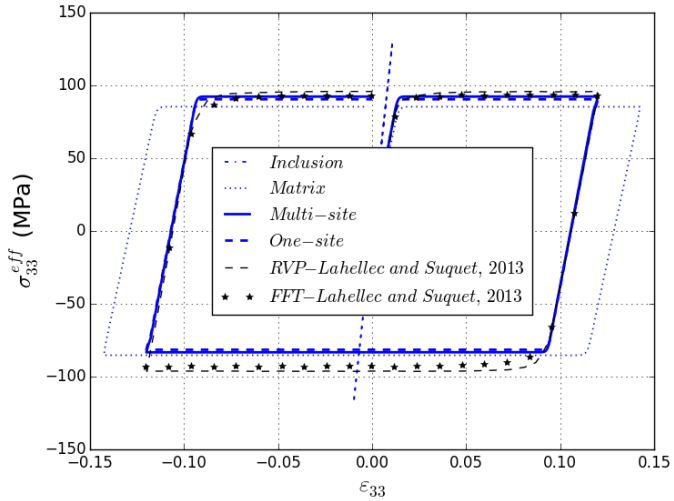

***Figure 10*** *Rate-dependent matrix. Radial loading–unloading Comparison between inclusion, matrix, one-site, multi-site, and Fig.10a Lahellec and Suquet [36] RVP and FFT models.*

### *3.1.2 Particles-reinforced polycarbonate matrix composites*

This composite has been studied by Miled et al. [56] in the framework of the incremental affine modelling of coupled viscoelastic–viscoplastic composites and finite element (FE) analysis. Table 2 shows the material properties of the composite.

***Table 2*** *Constitutive model parameters for particle inclusions and polycarbonate [56].*

| **Matrix (polycarbonate)** | | | | | | | **Particles** | |
|---|---|---|---|---|---|---|---|---|
| **Shear modulus $G$ (MPa)** | **Bulk modulus $K$ (MPa)** | **Hardening parameters** | | **Viscoplastic parameters** | | **Yield stress $\sigma_Y$ (MPa)** | **Young modulus $E$ (MPa)** | **Poisson's ratio $\nu$** |
| | | $k$ **(MPa)** | $n$ | $\kappa(s^{-1})$ | $m$ | | | |
| 1074 | 3222 | 150 | 0.43 | 150 | 5 | 35 | 76000 | 0.22 |

The current approaches are compared with the research conducted by Miled et al. [56], focusing on the uniaxial tension behaviour of a composite material consisting of an elasto-viscoplastic matrix reinforced with elastic particles, as depicted in Figure 11. The impact of the viscoplastic function parameter $m$ on the stress-strain relationship of the composite is analysed in Figure 11 (a) – (d), considering three values for the matrix viscoplastic exponent: $m$ = 1, 5, and 20.

The results illustrated in Figure 13 show that the composite's response becomes stiffer with increasing $m$ value, and the discrepancy between the current approaches and Miled et al. [56]'s work becomes more pronounced. Additionally, Figure 11 (a), Figure 11 (c) and Figure 11 (e) explore the influence of different volume fractions, while Figure 11 (a), Figure 11 (c) and Figure 11 (f) examine the effect of strain rate. It is evident that higher volume fractions and strain rates lead to a stiffer composite response.

The discrepancies between the current models and Miled et al. [56]'s work are attributed to the utilisation of different approaches in their respective studies. Despite the differences, it is noteworthy that the maximum normalised stress difference between the models remains consistently close to 0.5 at 0.05 strain, indicating a reasonable agreement between the two approaches.

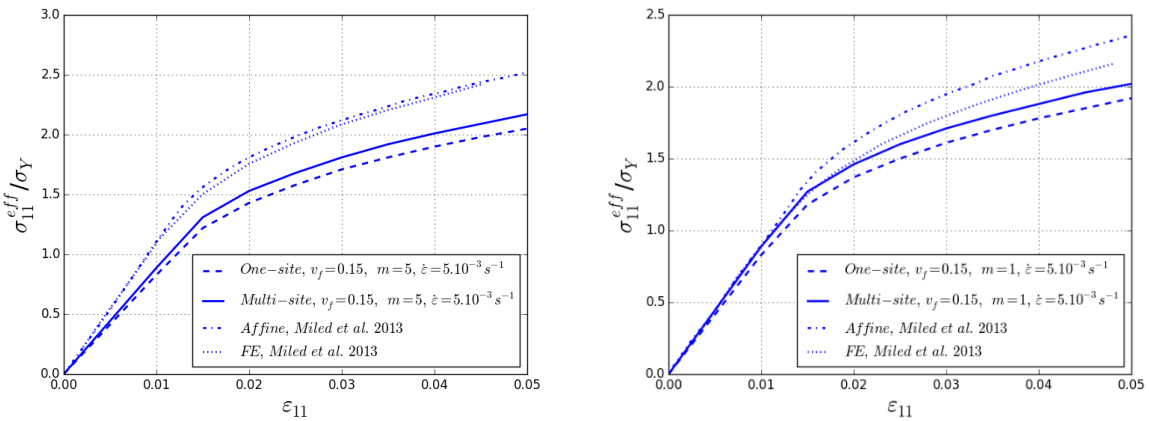

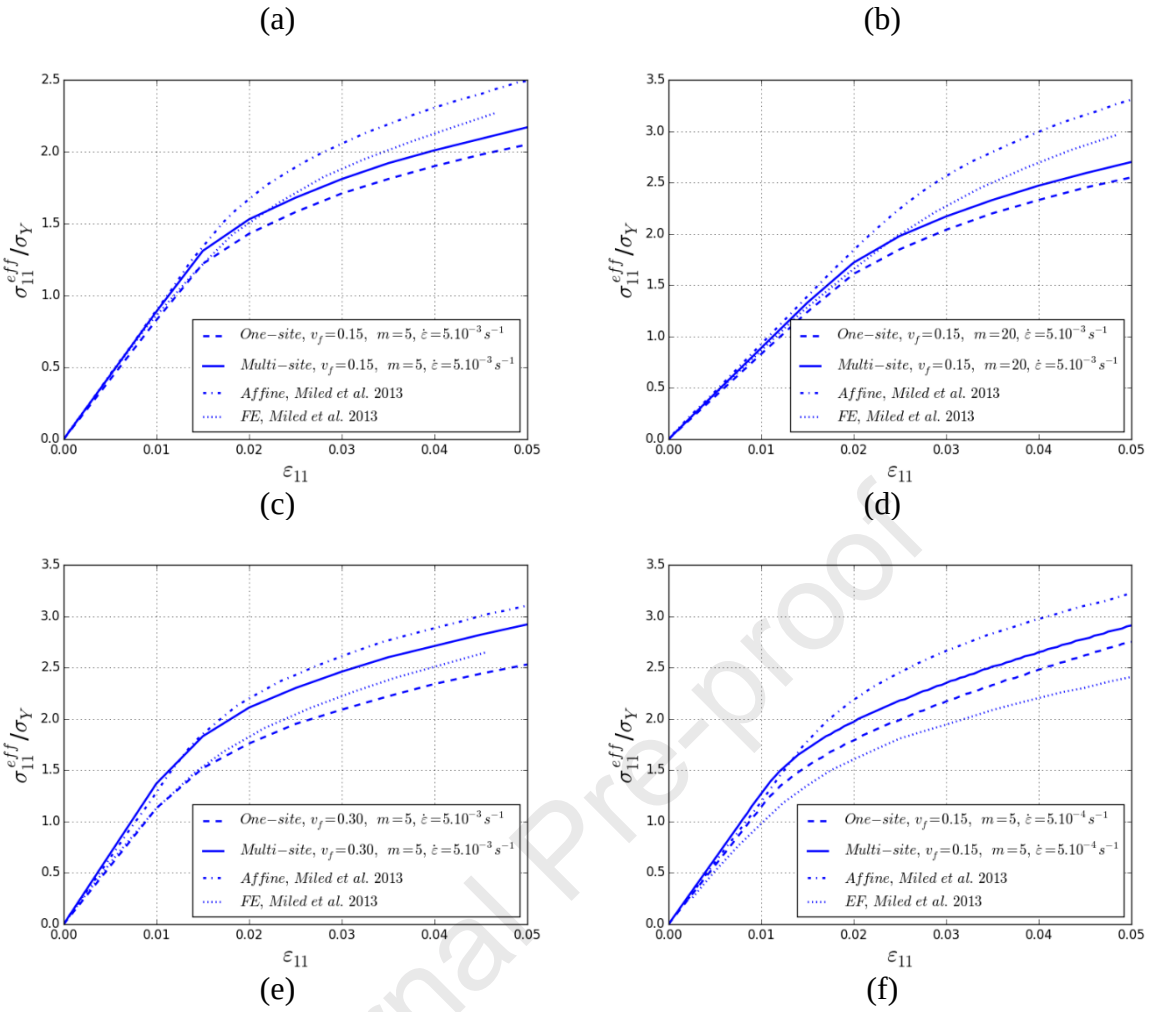


***Figure 11*** *Uniaxial tension of elasto-viscoplastic matrix reinforced with elastic particles using current approaches vs Miled et al. [56] FE and affine models:* (a) *Fig.7 Miled et al. with m=5&$v_f$=0.15,* (b) *Fig.9a Miled et al. with m=1&$v_f$=0.15,* (c) *Fig.9a Miled et al. with m =5&$v_f$=0.15,* (d) *Fig9a Miled et al. with m=20&$v_f$=0.15,* (e) *Fig.10b Miled et al. with m =5& $v_f$=0.3 and* (f) *Fig.11a Miled et al. with m=5& $v_f$=0.15.*

### *3.1.3 Comparison with experimental data*

One of the objectives of the created models is to design and anticipate the performance of biocomposite materials depending solely on available or predefined constituent material properties, eliminating the need for prior experimentation. However, it should be mentioned that only a broad overview or an idealistic biocomposite behaviour could be obtained. In practice, there are a number of factors involved that affect the behaviour of composite materials, as will be illustrated in the following comparison.

Under the consideration of devising a novel polylactic acid (PLA)/hemp biocomposite material, the data available in Table 3 are utilised. Experimental data of polylactic acid (PLA)/hemp biocomposite based on the work done by Mazzanti et al. [63] are considered.

***Table 3*** *Material properties for PLA/hemp constituent materials.*

| PLA matrix | | | | | | | | | |
|---|---|---|---|---|---|---|---|---|---|
| $E_{PLA}$ | $\nu_{PLA}$ | $\sigma_{PLA}$ | $k_{PLA}$ | $n_{PLA}$ | $\kappa_{PLA}$ [1/s] | $m_{PLA}$ | $S_{PLA}$ | $s_{PLA}$ | $\rho_{PLA}$ |
| 3.2 GPa | 0.35 | 15.0 MPa | 80 MPa | 0.2 | 150 | 10 | 2 MPa | 0.5 | 1.24 g/cm$^3$ |
| Hemp fibres | | | | | | | | | |
| $E_H$ | $\nu_H$ | $\sigma_H$ | $k_H$ | $n_H$ | $\kappa_H$ [1/s] | $m_H$ | $S_H$ | $s_H$ | AR | $\rho_H$ |
| 65.0 GPa | 0.27 | 150 MPa | 140 MPa | 0.3 | 150 | 5 | 2 MPa | 0.5 | 20 | 1. 5 g/cm$^3$ |

Figure 12 depicts the application of the present methodology and demonstrates the achievable outcomes concerning aligned or randomly oriented fibres. This is done in comparison with experimental data obtained from Mazzanti et al. [63] to elucidate the validity of the current model. Figure 12 (a) and (b) illustrate the scenario where the biocomposite is intended for reinforcement with aligned fibres, demonstrating the application of load in longitudinal and transverse directions, respectively. Meanwhile, Figure 12 (c) shows the situation when the biocomposite is configured with randomly oriented reinforced fibres.

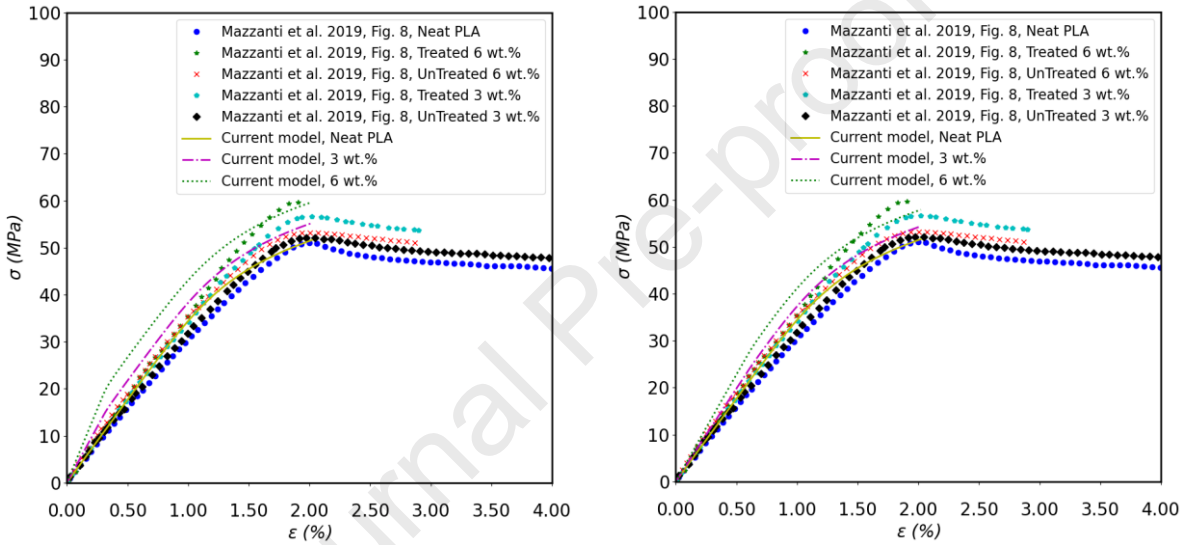


(a) (b)

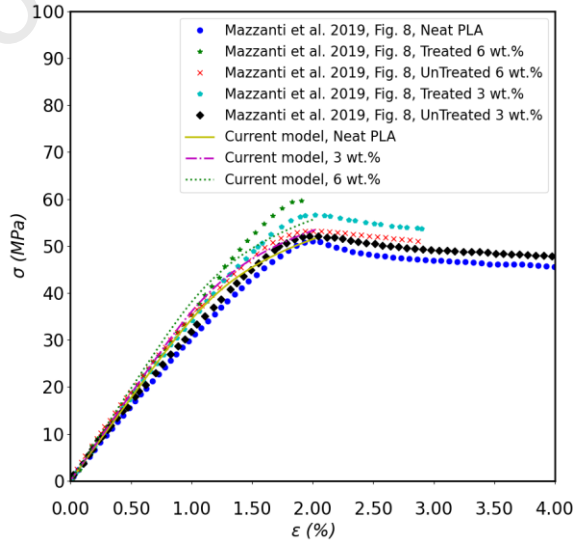


(c)

***Figure 12*** *Several design approaches for PLA/hemp biocomposite and their comparison with experimental data from Mazzanti et al. [63]* (a) *aligned fibres under longitudinal loading,* (b) *aligned fibre under transverse loading and* (c) *randomly-oriented fibres biocomposite.*

As per the information presented in Figure 12, the crucial consideration is not how perfect the match between the outcomes and experimental results is, but rather, it revolves around the accuracy with which the prediction aligns with the overall behaviour of the biocomposite. In reality, several parameters come into play, such as interfacial adhesion, chemical treatments (e.g. alkaline treatment), as in the current case by Mazzanti et al. [63] or the actual morphology or dispersion of fibres within the matrix, not to mention the factors affecting the polymer matrix itself (e.g. curing time and agents, catalysts, moisture sensitivity ). Given these considerations, the current model has effectively produced a rational prediction.

## 3.2 Application to bamboo/flax-reinforced epoxy composites

Flax/bamboo fibre-reinforced epoxy hybrid composites are utilised as an improvement to the physical and mechanical behaviour of biocomposite. The 3-phases flax/bamboo fibre-reinforced epoxy composites are modelled with different volume fractions. Although 2-phases flax epoxy composite has been reported to show higher strength than the 3-phases hybrid composites, flax/bamboo fibres reinforced epoxy shows high compatibility with resining [64, 65]. In addition to improvement in the mechanical and water absorption by combining two different natural fibres on the polymer resin [66].

Bamboo and flax are plant-based fibres that exhibit non-linear behaviours. Previous studies carried out on plant-based fibre-reinforced composites have shown that this non-linear behaviour is known to transfer to the composite and can mainly be attributed to viscoplastic effects [67, 68, 69, 70]. Thus, in the current study, the work was focused on modelling elasto–viscoplastic behaviour of the composite. For comparison purposes, two design criteria were followed. One criterion (criterion-I) considers all composite constituents to behave elasto–viscoplastically. The other (criterion-II) considers the matrix material the only elasto–viscoplastic phase, while reinforcement fibres are elastic.

Material properties for the bamboo and flax fibres, as well as matrix material, are illustrated in Table 4. Aligned fibre orientation is considered for the 3 phases biocomposite, which could be depicted by unidirectional RVEs, as shown in Figure 13. Mathematically, the uniformly distributed fibres and the multi-layered (laminates) fibre-reinforced biocomposite depicted in Figure 13 (a) and Figure 13 (b), respectively, may produce identical outcomes. However, considering manufacturing feasibility, the multi-layered fibre-reinforced biocomposite is more achievable.

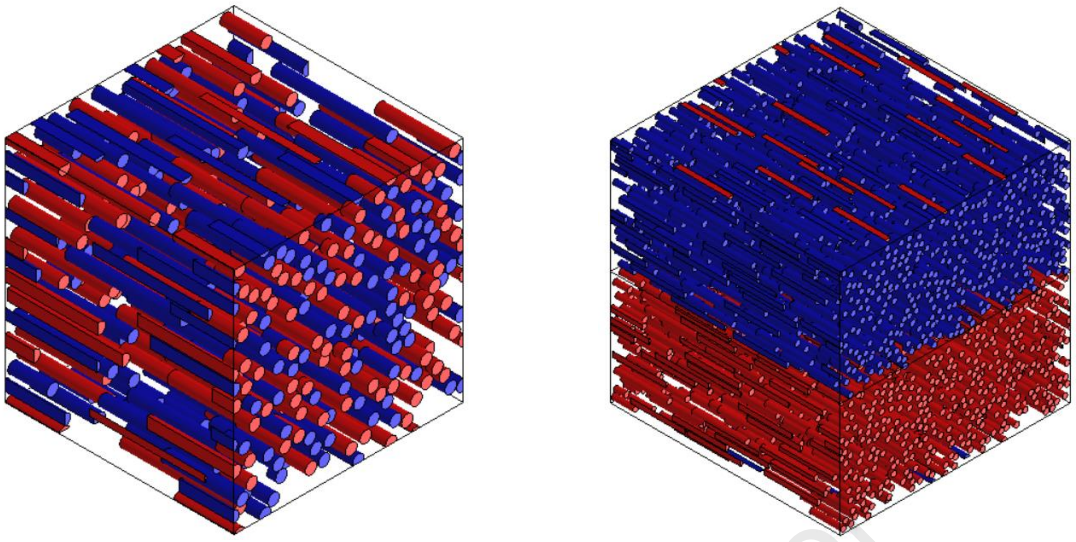

(a) (b)

***Figure 13*** *Unidirectional RVEs:* (a) *uniformly distributed fibres or* (b) *multi-layers of fibre-reinforced biocomposite*.

Figure 14 illustrates the composite behaviour using the one-site approach for different volume fractions. In Figure 14 (a), the analysis follows criterion-I, where all reinforcements and matrix are considered elasto-viscoplastic. On the other hand, in Figure 14 (b), the analysis follows criterion-II, where only the matrix is considered elasto-viscoplastic while all reinforcements are elastic. Similarly, Figure 15 illustrates the composite behaviour using the multi-site approach. It is evident that the overall composite response under criterion-II is much stiffer than for criterion-I, showing a much higher stress range.

***Table 4*** *Material properties for bamboo/flax/epoxy constituent materials [66, 71].*

| Epoxy matrix | | | | | | | | | | | |
|---|---|---|---|---|---|---|---|---|---|---|---|
| $E_E$ | $\nu_E$ | $\sigma_E$ | $k_E$ | $n_E$ | $\kappa_E$ [1/s] | $m_E$ | $S_E$ | $s_E$ | $\rho_E$ | $\alpha^{(E)}$ | |
| 2.2 GPa[a,b,c] | 0.35[b] | 53.5 MPa | 140 MPa | 0.33 | 150 | 10 | 2 MPa | 0.5 | 1.14 g/cm$^3$[d] | 9.9x10$^{-5}$ /$^o$C | |
| Flax fibres | | | | | | | | | | | |
| $E_x$ | $\nu_x$ | $\sigma_x$ | $k_x$ | $n_x$ | $\kappa_x$ [1/s] | $m_x$ | $S_x$ | $s_x$ | $\rho_x$ | $\alpha^{(x)}$ | AR |
| 82.5GPa[e] | 0.27 | 244 MPa | 200 MPa | 0.4 | 150 | 5 | 2 MPa | 0.5 | 1.45 g/cm$^3$[f] | 22.5x10$^{-6}$ /$^o$C | 10[g] |
| Bamboo fibres | | | | | | | | | | | |
| $E_B$ | $\nu_B$ | $\sigma_B$ | $k_B$ | $n_B$ | $\kappa_B$ [1/s] | $m_B$ | $S_B$ | $s_B$ | $\rho_B$ | $\alpha^{(B)}$ | AR |
| 21.5 GPa[e] | 0.39 | 39.9 MPa | 63 MPa | 0.35 | 150 | 5 | 2 MPa | 0.5 | 0.85 g/cm$^3$[f] | 3.35x10$^{-6}$ /$^o$C | 10[h] |

[a] Tzetzis et al. [72]
[b] Essmeister et al. [73]
[c] Sajjad el al. [74]
[d] Oral et al. [75]
[e] Akampumuza et al. [71]
[f] Dittenber and GangaRao [76]
[g] Bos et al. [77]
[h] Maier et al. [78]

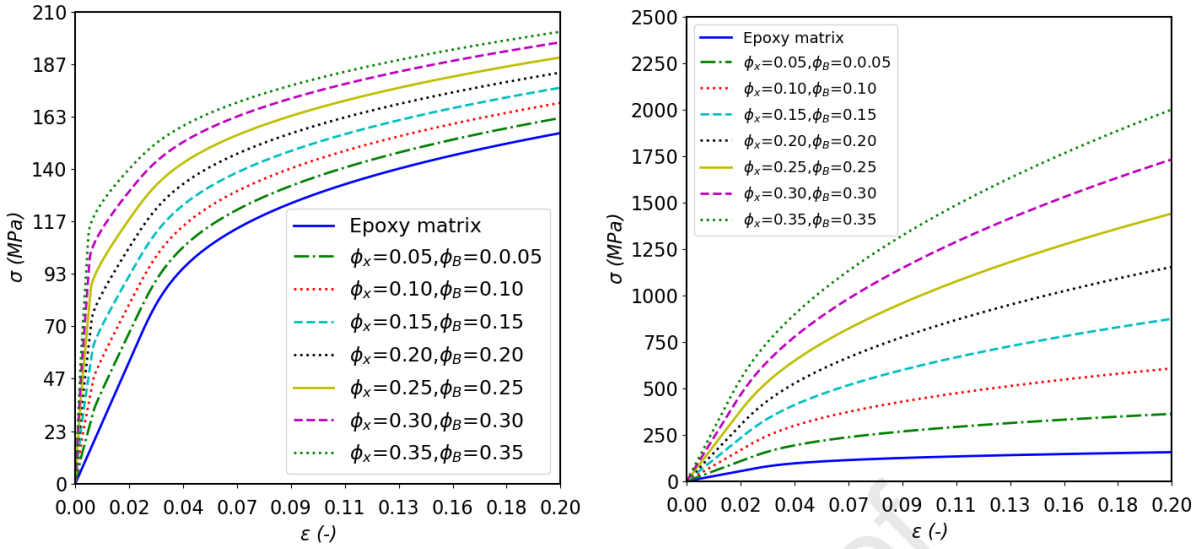


(a) (b)

***Figure 14*** *Effect of volume fractions at strain rate ($\dot{\varepsilon}$)=$10^{-4}$ using one-site modelling:* (a) *elasto-viscoplastic matrix & reinforcements, and* (b) *elasto-viscoplastic matrix with elastic reinforcements.*

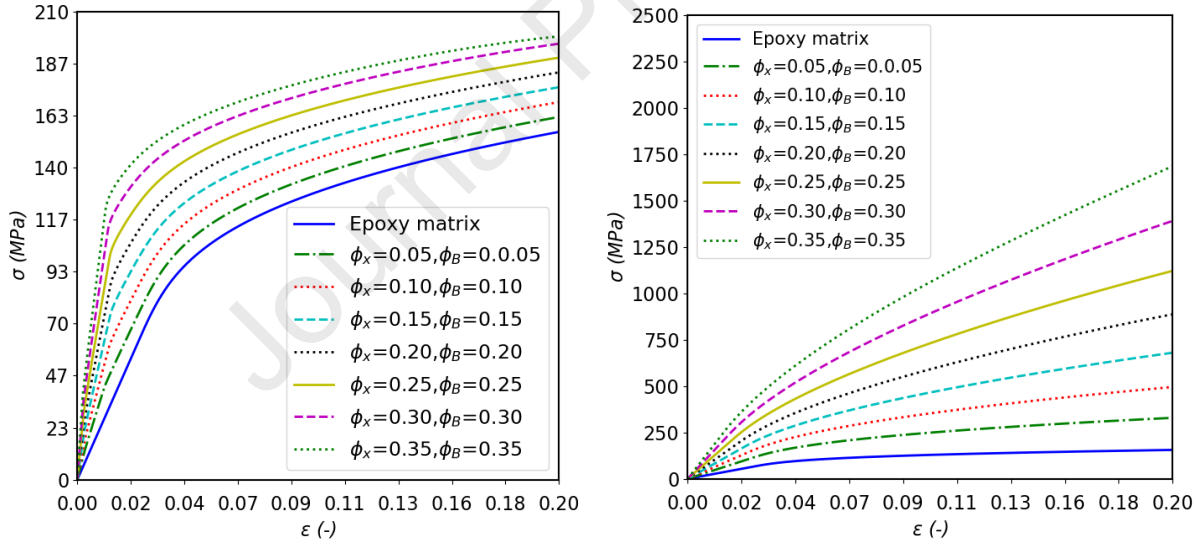


(a) (b)

***Figure 15*** *Effect of volume fractions at strain rate ($\dot{\varepsilon}$)=$10^{-4}$ using multi-site modelling:* (a) *elasto-viscoplastic matrix & reinforcements, and* (b) *elasto-viscoplastic matrix with elastic reinforcements.*

Figure 16 directly compares the composite behaviour using one- and multi-site approaches. Figure 16 (a) shows that they have identical responses outside the elastic zone under criterion-I. However, Figure 16 (b) illustrates that the discrepancy between the two models keeps increasing with increasing the volume fractions, where the one-site approach shows a stiffer response than the multi-site model. This is indicated by the difference in stress level between the two approaches, which becomes more pronounced at specific strain points as the composite

material's volume fraction varies. For example, at a strain of 0.2, the stress exhibits an increase of 16.6, 33.33, and 23.4% when utilising the one-site approach compared to the multi-site approach for volume fractions of 0.1, 0.2, and 0.3, respectively.

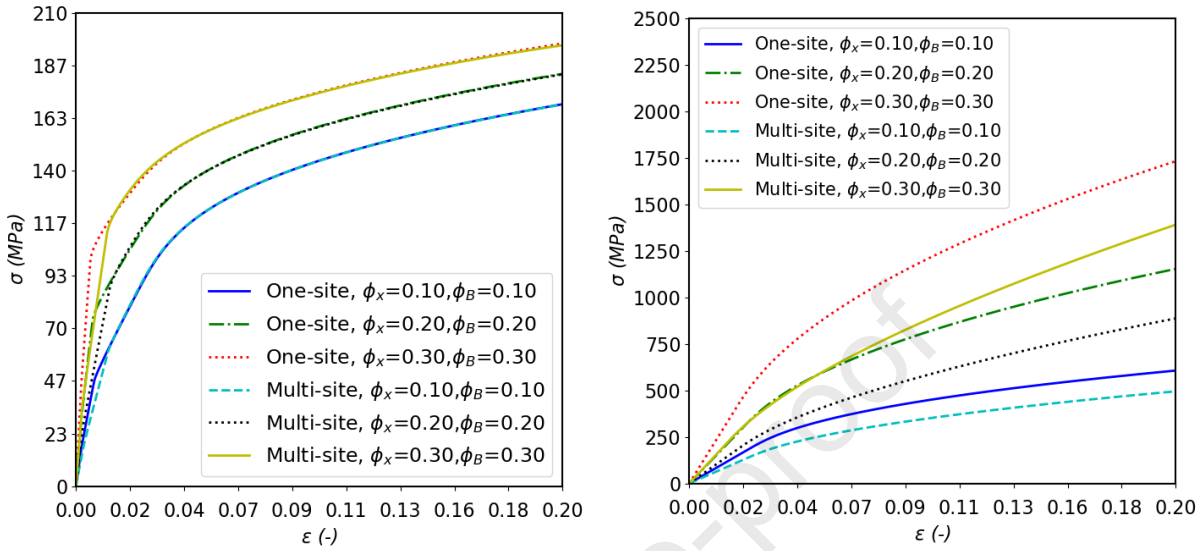


***Figure 16*** *One-site vs multi-site modelling at strain rate ($\dot{\varepsilon}$)=$10^{-4}$ :* (a) *elasto-viscoplastic matrix & reinforcements, and* (b) *elasto-viscoplastic matrix with elastic reinforcements.*

## 3.3 Finite element analysis (FEA)

### *3.3.1 Failure criteria considered when devising a new untested biocomposite*

In the assessment of a novel and untested biocomposite intended for a specific application, it becomes imperative to define criteria for material failure. The existing approach involves the application of the erosion concept (element deletion technique) [79, 80] , wherein elements within the Finite Element (FE) model are systematically deleted to emulate total material failure. This deletion process is triggered when the strength of the equivalent biocomposite surpasses a predetermined erosion threshold, as elucidated in the Finite Element Analysis (FEA) algorithm explicated in Figure 5.

This strength needs to be experimentally determined. Conducting experimental strength measurements yields more accurate results, given the multitude of physical factors influencing the failure of composite materials.

Nevertheless, it is proposed that initially, in the design phase, numerical characterisation could serve as a simplified substitute before the commencement of any experimental investigations.

The challenge arises in determining this erosion threshold value, and the most pragmatic solution lies in numerically deriving these thresholds. One method of material characterisation

utilised for this determination involves the execution of tensile tests, a process elaborated upon in the subsequent subsection of section 3.3.2. This methodological step is instrumental in facilitating the identification and quantification of virtual damage/failure thresholds.

### *3.3.2 Tensile testing*

In this subsection, two procedures are undertaken to study the hybrid composite material: finite element (FE) computations and results' verification. First, finite element (FE) tensile testing is performed on the hybrid composite to assess its mechanical behaviour, and second, results from the computational FE analysis are compared with results obtained using analytical analysis to verify their accuracy and reliability. In Figure 17, the stress distribution on the meshed model is depicted, considering criterion-I. It is evident that the stress distribution obtained using the one-site approach is noticeably higher than that of the multi-site approach. Furthermore, a close agreement between the FE and analytical results is demonstrated on the stress-strain curves, confirming the accuracy of the FE computations. Likewise, similar observations are made in Figure 18, where criterion-II is considered. The stress distribution analysis shows the same trend, with the one-site approach resulting in higher stress values compared to the multi-site approach. Moreover, the stress-strain curves obtained from the FE computations and the analytical analysis exhibit an excellent match, further validating the accuracy and consistency of the FE results.

The successful comparison between the FE computations and the analytical analysis reinforces the confidence in the chosen approaches and their capability to provide reliable insights into the mechanical behaviour of the hybrid composite material under loading conditions.

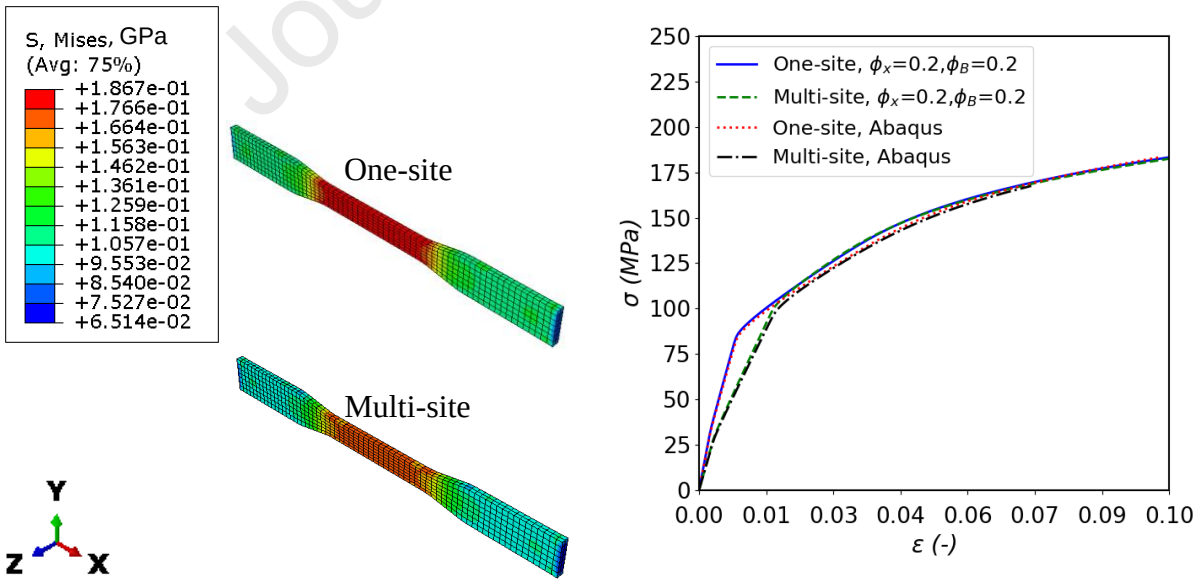


***Figure 17*** *FE and analytical tensile testing for elasto-viscoplastic matrix & reinforcements at strain rate* $(\dot{\varepsilon})=10^{-1}$.

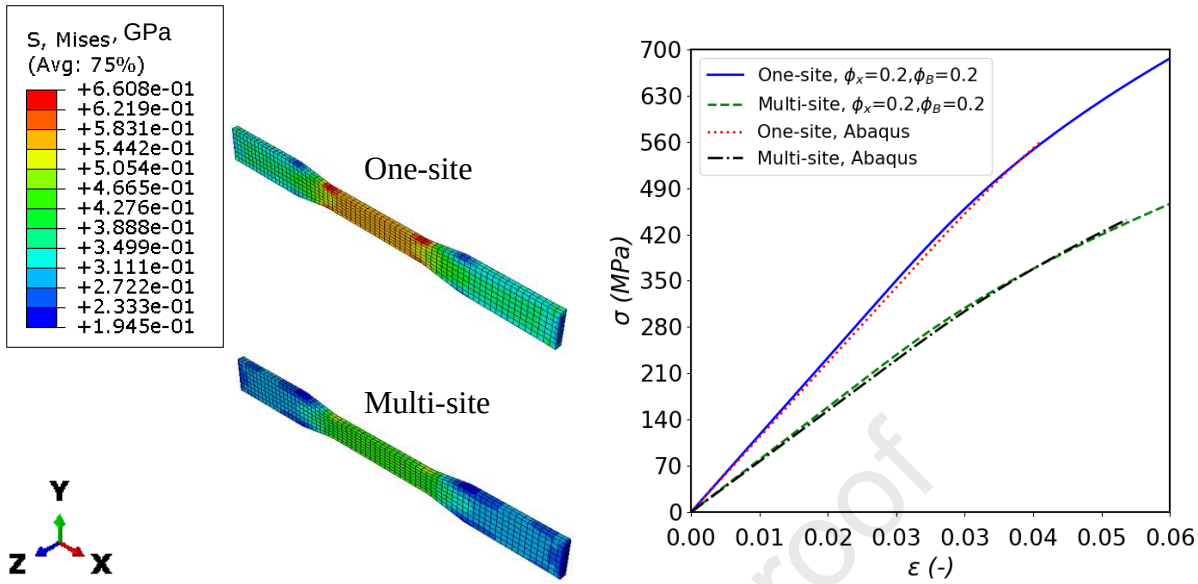


***Figure 18*** *FE and analytical tensile testing for elasto-viscoplastic matrix with elastic reinforcements at strain rate ($\dot{\varepsilon}$)=$10^{-1}$.*

### *3.3.3 Bending test*

A 3-point bending models are used to asses stiffness of biocomposite panels. They are evaluated using one-site criterion-I and -II modelling approaches. Chemical treatments have the potential to impact the mechanical and physical properties of plant-based fibres in biocomposite materials, leading to variations in their mechanical behaviour and the manifestation of specific characteristics [81, 82, 83]. Consequently, a single biocomposite material may exhibit diverse behaviours, such as those aligned with criterion-II or criterion-I.

Figure 19 shows the stress distribution and plots of the flexural force against deflection considering longitudinal fibre orientations. As illustrated, designing and manufacturing the biocomposite material according to criterion-II offers superior energy absorption capabilities, making it more suitable for scenarios where enhanced construction is of paramount importance. On the other hand, criterion-I results in more pronounced ductility to the structure, which could be beneficial in certain situations to effectively dissipate impact forces.

The choice between design approaches for the biocomposite material will largely depend on the effect of chemical treatment influenced by factors, such as the type of fibre, the specific chemical treatment applied, and the treatment conditions as well as the particular design requirements.

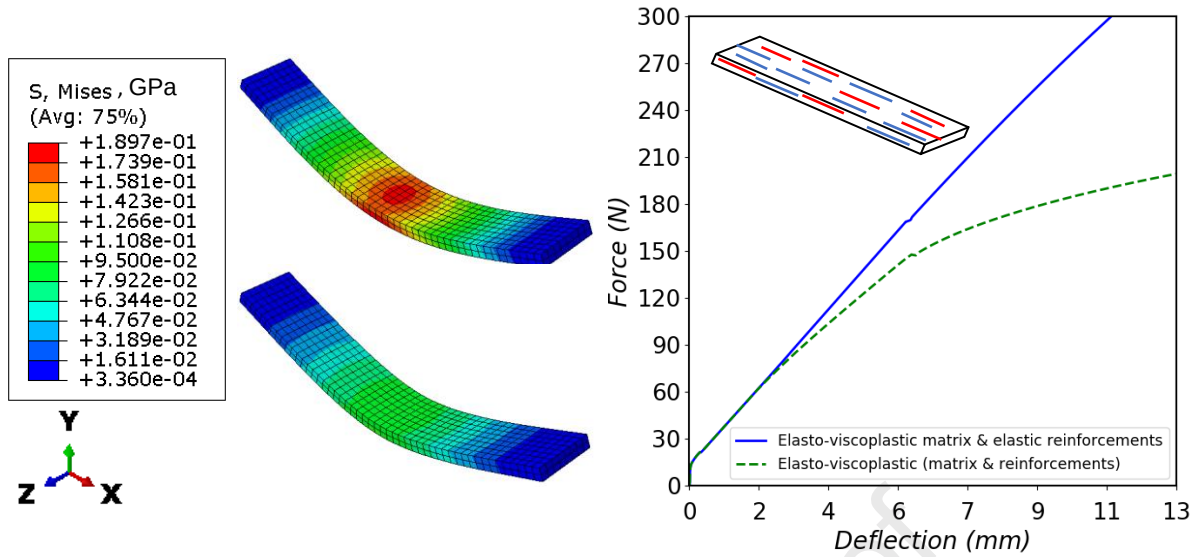


808 ***Figure 19*** *Stress distribution for bending of longitudinal fibres panel with* $\phi_x$*=0.2 and*
809 $\phi_B$*=0.2.*

810 Figure 20 demonstrates the stress distribution and the bending force-deflection curves
811 considering transverse fibre orientations. There is no pronounced difference in this case. This
812 outcome is anticipated, given that the load-bearing nature is more likely to be influenced by the
813 matrix rather than the fibres.

814

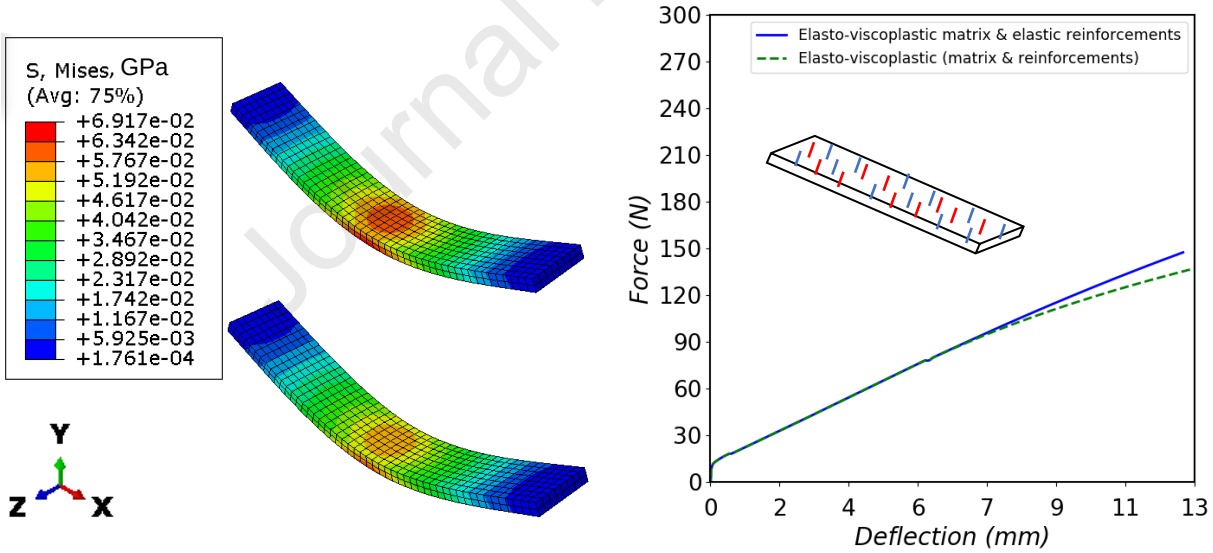


815 ***Figure 20*** *Stress distribution for bending of transverse fibres panel with* $\phi_x$*=0.2 and* $\phi_B$*=0.2.*

816

817 ## 3.4 Automotive and motorsport applications

818 Natural fibre composites are used to reduce waste. Bamboo-based hybrid composites and
819 hybrid composites based on epoxy and flax are used to manufacture high-strength panels [84,
820 85]. Thus, these composites represent potential green candidates as efficient automotive
821 structural components.

The rigidity and stiffness of a motorsport chassis are pivotal attributes influencing its overall performance and safety. Additionally, chassis robustness is integral to ensuring optimal chassis resistance against deformation or flexing under applied loads, stability and control during dynamic manoeuvres, and withstanding external forces without excessive elastic deformation. Three types of chassis design are commonly employed in motorsports: the space frame, typically constructed with steel tubular bar elements, the monocoque, made from metallic or conventional composite materials, and a hybrid design that combines elements of both space frame and monocoque construction. A biocomposite full motorsport monocoque chassis structure is considered herein as an application in order to assess its deformability and behaviour and give engineers and designers an edge to make informed decisions based on the desired trade-offs between absorbed energy and structural deformation. As can be seen, Figure 21 provides a comprehensive depiction of the stress distribution and deformation morphologies observed under criterion-II. While Figure 22 offers a comparative analysis by illustrating the same characteristics under criterion-I. The deformation area in Figure 22 appears to be more localised, and the stress deformation zone is more elongated. Additionally, Figure 23 presents the force versus deflection curve. The illustration exhibits a load-softening phenomenon [86, 87, 88] characterised by a predominantly elastic increase in load until reaching the initial flexural failure load. At this point, there is an abrupt decrease in load, succeeded by a subsequent ascent in a post-elastic stage.Here, it is evident that the force trend experiences an increase in magnitude with distance, particularly in scenarios governed by criterion-II. This observation underscores the critical role of criterion-II in influencing the mechanical response and performance of the chassis structure, highlighting its implications for structural design and rigidity.

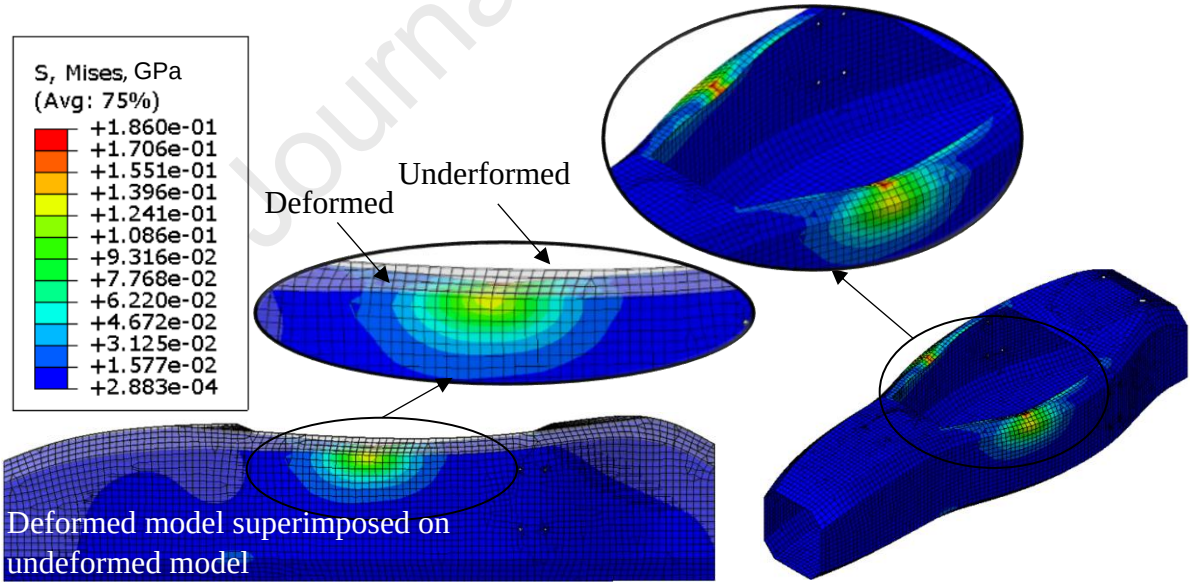


***Figure 21*** *Stress distribution for deformation of motorsport vehicle monocoque chassis structure of elasto-viscoplastic matrix with elastic reinforcements with* $\phi_x$*=0.2 and* $\phi_B$*=0.2.*

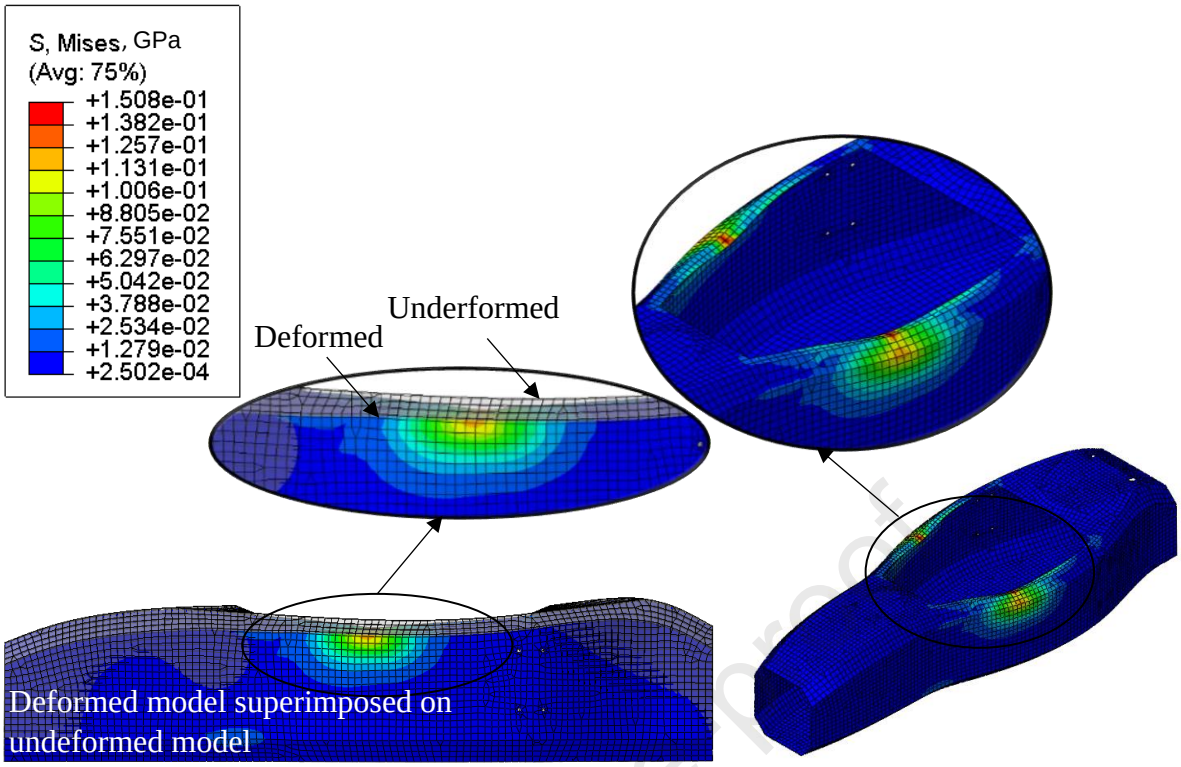


***Figure 22*** *Stress distribution for deformation of motorsport vehicle monocoque chassis structure of elasto-viscoplastic matrix & reinforcements with $\phi_x$=0.2 and $\phi_B$=0.2.*

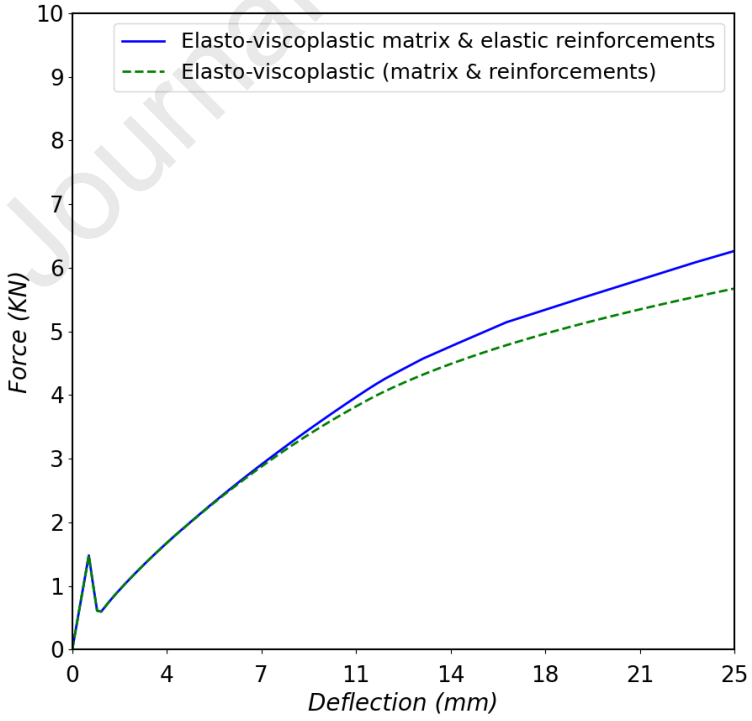


***Figure 23*** *Force verus deflection distribution for deformation of motorsport vehicle monocoque chassis structure with $\phi_x$=0.2 and $\phi_B$=0.2.*

# 4 Discussion

The present methodology has undergone validation against established theoretical outcomes, consistently demonstrating a good agreement. Furthermore, a comparison demonstration with experimental data was executed where the current models were employed to design and predict the performance of biocomposite materials, relying only on available or predetermined constituent material properties. This aims to underscore the model's validity in predicting a novel biocomposite, thereby obviating the necessity for preliminary experimentation. The demonstration emphasises the accuracy with which predictions align with the overall behaviour of the biocomposite, acknowledging the potential influence of various factors in reality, such as fibre morphology, chemical treatment, dispersion, moisture absorption and interfacial bonding strength.

Afterwards, the model was utilised to devise a 3 phases bamboo/flax hybrid biocomposite material. However, up to that point, the aspect of failure (rupture) had not been addressed. The analysis conducted thus far was only analytical, relying on constant mathematical uniaxial loading for a parametric study of the material's behaviour, elucidated by the high strains in Figure 14-19.

The introduction of the failure criterion occurs when experimental testing is conducted to determine the composite material's strength. Nevertheless, for this occasion, particularly during the initial design phase, a virtual failure criterion can be employed by incorporating the model as a user material subroutine (UMAT) in the Finite Element (FE) solver, as elaborated further in subsection 3.3.1.

The model is then successfully implemented as a UMAT within Abaqus FE solver. Numerical tensile characterisations, conducted in accordance with ASTM standards, were employed to validate analytical and computational outcomes. Furthermore, 3-point bending tests were also modelled following ASTM standards. These tests contribute to the identification of virtual damage and failure thresholds essential for simulating a full motorsport vehicle monocoque chassis structure deformation behaviour response.

Subsequently, numerical simulation of the bamboo/flax hybrid biocomposite material was considered for leveraging biocomposites in the construction of motorsport vehicle full monocoque chassis structure, which holds promise for total predictive modelling and can contribute to the overall structural integrity and safety of motorsport vehicles chassis. At the same time, shedding more light on biocomposite materials utilisations for such applications, which are different from conventional composites, and could result in varying inherent properties and a significant variation in behaviours, necessitating careful consideration during the selection and design phases of biocomposites. This initiative serves as a foundational step, emphasising a comprehensive reliance on numerical simulation for end-to-end modelling assessment and the incorporation of biocomposite materials in future vehicle manufacturing. The anticipated benefits include cost reduction, time efficiency, and, notably, alignment with environmental regulations.

# 5 Conclusion

A predictive material model that represents the behaviour of a multiphase bio-based composite is developed utilising bamboo/flax fibres reinforced epoxy. Two approaches, one-site and multi-site, were considered for modelling the biocomposite behaviour. The one-site approach considers certain assumptions and simplifications in modelling the composite behaviour. In contrast, the multi-site approach incorporates a more complex and comprehensive analysis by considering the interaction between inclusions and their surrounding neighbourhood that might influence the material's response. Moreover, a detailed calculation of the interaction tensor is presented along with its numerical implementation. The nonlinear response of the hybrid composite is derived under a rate dependent viscoplastic equations for which a regulated tangent operator is obtained for homogenisation purpose.

Based upon the results obtained, the following remarks can be made:

a) Comprehensive assessment and validation against existing literature demonstrate good agreement.
b) Based on experimental results reported in the literature, the observed difference between predicted and experimental outcomes can be ascribed to multiple factors, such as interfacial adhesion, chemical treatments, and other pertinent parameters.
c) Consequently, a single biocomposite material may exhibit diverse behaviours variations in their mechanical behaviour as a result, the same biocomposite material may exhibit diverse behaviours.
d) Accordingly, the bamboo/flax fibres reinforced epoxy hybrid composite behaviour was modelled under two criterions-I and II, when utilising the one-site and multi-site approaches. One-site approach exaggerates results compared to multi-site results under criterion-II.
e) Computational FE analysis results were compared with analytical analysis to ensure accuracy and reliability, which yielded an excellent match.
f) The establishment of the failure criterion requires experimental determination. However, a virtual failure criterion can be utilised in the preliminary stages of design.
g) The deformability of the hybrid biocomposite was successfully exhibited for the motorsport vehicle's full monocoque chassis structure, providing valuable insights into its performance. Nevertheless, the selection of design methodologies for the biocomposite material will predominantly hinge on the manufacturing process, subsequent processes, treatment conditions applied to the biocomposite, and the specific design criteria for the motorsport structural components.

# References

[1] S. Mishra, A. Mohanty, L. Drzal, M. Misra, S. Parija, S. Nayak and S. Tripathy, “Studies on mechanical performance of biofibre/glass reinforced polyester hybrid composites,” *Composites Science and Technology*, vol. 63, no. 10, pp. 1377-1385, 2003.

[2] A. L. Duigou, A. Bourmaud, C. Gourier and C. Baley, "Multi-scale shear properties of flax fibre reinforced polyamide 11 biocomposites," *Composites Part A: Applied Science and Manufacturing,* vol. 85, pp. 123-129, 2016.

[3] B. Zuccarello and R. Scaffaro, "Experimental analysis and micromechanical models of high performance renewable agave reinforced biocomposites," *Composites Part B: Engineering,* vol. 119, no. 1359-8368, pp. 141-152, 2017.

[4] M. J. John and S. Thomas, "Biofibres and biocomposites," *Carbohydrate Polymers,* vol. 71, no. 3, pp. 343-364, 2008.

[5] G. Nehls, "Natural fiber crash box design for motorsport," CompositesWorld, 23 October 2020. [Online]. Available: https://www.compositesworld.com/news/natural-fiber-crash-box-design-for-motorsport.

[6] G. Nehls, "McLaren, Bcomp use natural composite fibers in F1 racing seat," CompositesWorld, 3 September 2020. [Online]. Available: https://www.compositesworld.com/news/mclaren-bcomp-uses-natural-composite-fibers-in-f1-racing-seat.

[7] G. Nehls, "Porsche, Bcomp collaborate on racing car with all-natural fiber composite bodywork," CompositesWorld, 1 October 2020. [Online]. Available: https://www.compositesworld.com/news/porsche-bcomp-collaborate-on-racing-car-with-all-natural-fiber-composite-bodywork-.

[8] R. Eshkoor, S. Oshkovr, A. Sulong, R. Zulkifli, A. Ariffin and C. Azhari, "Comparative research on the crashworthiness characteristics of woven natural silk/epoxy composite tubes," *Materials & Design,* vol. 47, pp. 248-257, 2013.

[9] R. Eshkoor, S. Oshkovr, A. Sulong, R. Zulkifli, A. Ariffin and C. Azhari, "Effect of trigger configuration on the crashworthiness characteristics of natural silk epoxy composite tubes," *Composites Part B: Engineering,* vol. 55, pp. 5-10, 2013.

[10] R. Eshkoor, A. Ude, A. Sulong, R. Zulkifli, A. Ariffin and C. Azhari, "Energy absorption and load carrying capability of woven natural silk epoxy–triggered composite tubes," *Composites Part B: Engineering,* vol. 77, pp. 10-18, 2015.

[11] R. A. Eshkoor, A. U. Ude, S. A. Oshkovr, A. B. Sulong, R. Zulkifli, A. K. Ariffin and C. H. Azhari, "Failure mechanism of woven natural silk/epoxy rectangular composite tubes under axial quasi-static crushing test using trigger mechanism," *International Journal of Impact Engineering,* vol. 64, pp. 53-61, 2014.

[12] S. Ataollahi, S. Taher, R. Eshkoorl, A. Ariffin and C. Azhari, "Energy absorption and failure response of silk/epoxy composite square tubes: Experimental," *Composites Part B: Engineering,* vol. 43, no. 2, pp. 542-548, 2012.

[13] A. U. Ude, R. A. Eshkoor and C. H. Azhari, "Crashworthy characteristics of axial quasi-statically compressed Bombyx mori composite cylindrical tubes: Experimental," *Fibers and Polymers,* vol. 18, no. 8, pp. 1594-1601, 2017.

[14] L. Y. a. N. Chouw, "Crashworthiness characteristics of flax fibre reinforced epoxy tubes for energy absorption application," *Materials & Design,* vol. 51, pp. 629-640, 2013.

[15] J. Hu, S. Yin, T. Yu and J. Xu, "Dynamic compressive behavior of woven flax-epoxy-laminated composites," *International Journal of Impact Engineering,* vol. 117, pp. 63-74, 2018.

[16] L. Yan, N. Chouw and K. Jayaraman, "Effect of triggering and polyurethane foam-filler on axial crushing of natural flax/epoxy composite tubes," *Materials & Design (1980-2015),* vol. 56, pp. 528-541, 2014.

[17] D. Tomlinson and A. Fam, "Axial response of flax fibre reinforced polymer-skinned tubes with lightweight foam cores and bioresin blend," *Thin-Walled Structures,* vol. 155, p. 106923, 2020.

[18] A. Mache, A. Deb and N. Gupta, "An experimental study on performance of jute-polyester composite tubes under axial and transverse impact loading," *Polymer Composites,* vol. 41, no. 5, pp. 1695-2119, 2020.

[19] R. Sivagurunathan, S. L. T. Way, L. Sivagurunathan and M. Y. Yaakob, "The Effects of Triggering Mechanisms on the Energy Absorption Capability of Circular Jute/Epoxy Composite Tubes under Quasi-Static Axial Loading," *Applied Composite Materials,* vol. 25, no. 6, pp. 1401-1417, 2018.

[20] Z. F. Albahash and M. Ansari, "Investigation on energy absorption of natural and hybrid fiber under axial static crushing," *Composites Science and Technology,* vol. 151, pp. 52-61, 2017.

[21] M. A. Attia, M. A. A. El–Baky, M. A. Hassan, T. A. Sebaey and E. Mahdi, "Crashworthiness characteristics of carbon–jute–glass reinforced epoxy composite circular tubes," *Polymer Composites,* vol. 39, no. S4, pp. E1951-E2610, 2018.

[22] A. Supian, S. Sapuan, M. Zuhri, E. Zainudin and H. Ya, "Crashworthiness performance of hybrid kenaf/glass fiber reinforced epoxy tube on winding orientation effect under quasi-static compression load," *Defence Technology,* vol. 16, no. 5, pp. 1051-1061, 2020.

[23] A. P. Kumar, M. Shunmugasundaram, S. Sivasankar and L. P. Sankar, "Static axial crushing response on the energy absorption capability of hybrid Kenaf/Glass fabric cylindrical tubes," *Materials Today: Proceedings,* vol. 27, pp. 783-787, 2020.

[24] M. J. Ghoushji, R. A. Eshkoor, R. Zulkifli, A. B. Sulong, S. Abdullah and C. H. Azhari, "Energy Absorption Capability of Axially Compressed Woven Natural Ramie/Green Epoxy Square Composite Tubes," *Journal of Reinforced Plastics and Composites,* vol. 36, no. 14, pp. 1028-1037, 2017.

[25] E. Mahdi, D. Ochoa, A. Vaziri and E. Eltai, “Energy absorption capability of date palm leaf fiber reinforced epoxy composites rectangular tubes,” *Composite Structures,* vol. 224, p. 111004, 2019.

[26] M. Alkateb, S. Sapuan, Z. Leman, M. Jawaid and M. Ishak, “Crushing behavior of kenaf fiber/wooden stick reinforced epoxy hybrid "green”composite elliptical tubes,” *Polimery,* vol. 63, no. 6, pp. 436-443, 2018.

[27] “Promoting sustainable development with advanced bio-based composites,” EU Horizon 2020-funded SSUCHY, 2022. [Online]. Available: https://cordis.europa.eu/article/id/428543-promoting-sustainable-development-with-advanced-bio-based-composites.

[28] “Advanced BIObased polyurethanes and fibres for the autoMOTIVE industry with increased environmental sustainability,” EU Horizon 2020-funded BIOMOTIVE, 2021. [Online]. Available: https://cordis.europa.eu/project/id/745766.

[29] “FIBERGREEN PROJECT,” IGESTEK, 2020. [Online]. Available: https://igestek.com/fibergreen-project/.

[30] “Revealed: How McLaren is pioneering the use of sustainable composites in F1,” McLaren, 18 August 2020. [Online]. Available: https://www.mclaren.com/racing/sustainability/natural-fibre-sustainable-composite-racing-seat/.

[31] E. Mahdi, A. Mokhtar, N. Asari, F. Elfaki and E. Abdullah, “Nonlinear finite element analysis of axially crushed cotton fibre composite corrugated tubes,” *Composite Structures,* vol. 75, no. 1-4, pp. 39-48, 2006.

[32] S. Oshkovr, S. Taher, A. Oshkour, A. Ariffin and C. Azhari, “Finite element modelling of axially crushed silk/epoxy composite square tubes,” *Composite Structures,* vol. 95, pp. 411-418, 2013.

[33] O. Pierard, J. LLorca, J. Segurado and I. Doghri, “Micromechanics of particle-reinforced elasto-viscoplastic composites: Finite element simulations versus affine homogenization,” *International Journal of Plasticity,* vol. 23, no. 6, pp. 1041-1060, 2007.

[34] L. Zhang and W. Yu, “A micromechanics approach to homogenizing elasto-viscoplastic heterogeneous materials,” *International Journal of Solids and Structures,* vol. 51, no. 23-24, pp. 3878-3888, 2014.

[35] S. Marfia and E. Sacco, “Multiscale technique for nonlinear analysis of elastoplastic and viscoplastic composites,” *Composites Part B: Engineering,* vol. 136, pp. 241-253, 2018.

[36] N. Lahellec and P. Suquet, “Effective response and field statistics in elasto-plastic and elasto-viscoplastic composites under radial and non-radial loadings,” *International Journal of Plasticity,* vol. 42, pp. 1-30, 2013.

[37] K. Kowalczyk-Gajewska, M. Majewski, S. Mercier and A. Molinari, "Mean field interaction model accounting for the spatial distribution of inclusions in elastic-viscoplastic composites," *International Journal of Solids and Structures,* vol. 224, p. 111040, 2021.

[38] A. Molinari and M. E. Mouden, "The problem of elastic inclusions at finite concentration," *International Journal of Solids and Structures,* vol. 33, no. 20-22, pp. 3131-3150, 1996.

[39] O. Fassi-Fehri, "Le probléme de la paire d'inclusions plastiques et hétérogénes dans une matrice anisotrope: application á l'étude du comportement des matériaux composites et de la plasticité (Ph.D. thesis)," 1985.

[40] O. Fassi-Fehri, A. Hihi and M. Berveiller, "Multiple site self consistent," *International Journal of Engineering Science,* vol. 27, no. 5, pp. 495-502, 1989.

[41] A. Broohm, P. Zattarin and P. Lipinski, "Prediction of mechanical behaviour of inhomogeneous and anisotropic materials using an incremental scheme," *Archives of Mechanics,* vol. 52, no. 6, pp. 949-967, 2000.

[42] J. W. Ju and T. M. Chen, "Effective Elastic Moduli of Two-Phase Composites Containing Randomly Dispersed Spherical Inhomogeneities," *Acta Mechanica,* vol. 103, no. 1-4, pp. 123-144, 1994.

[43] J. W. Ju and T. M. Chen, "Micromechanics and Effective Moduli of Elastic Composites Containing Randomly Dispersed Ellipsoidal Inhomogeneities," *Acta Mechanica,* vol. 103, no. 1-4, pp. 103-121, 1994.

[44] J. Ju and K. Tseng, "Effective elastoplastic behavior of two-phase ductile matrix composites: A micromechanical framework," *International Journal of Solids and Structures,* vol. 33, no. 29, pp. 4267-4291, 1996.

[45] J. Ju and L. Sun, "Effective elastoplastic behavior of metal matrix composites containing randomly located aligned spheroidal inhomogeneities. Part I: micromechanics-based formulation," *International Journal of Solids and Structures,* vol. 38, pp. 183-201, 2001.

[46] L. Z. Sun and J. W. Ju, "Effective elastoplastic behavior of metal matrix composites containing randomly located aligned spheroidal inhomogeneities. Part II: Applications," *International Journal of Solids and Structures,* vol. 38, pp. 203-225, 2001.

[47] W. Kpobie, S. B. Khlifa, N. Bonfoh, M. Fendler and P. Lipinski, "Multi-site micromechanical modelling of thermo-elastic properties of heterogeneous materials," *Composite Structures,* vol. 94, no. 6, pp. 2068-2077, 2012.

[48] W. Azoti, Y. Koutsawa, A. Tchalla, A. Makradi and S. Belouettar, "Micromechanics-based multi-site modeling of elastoplastic behavior of composite materials," *International Journal of Solids and Structures,* vol. 59, pp. 198-207, 2015.

[49] A. Elmasry, W. Azoti, M. Elmarakbi and A. Elmarakbi, "Interaction modelling of the thermomechanical behaviour of spatially-oriented graphene platelets (GPLs) reinforced polymer matrix," *International Journal of Solids and Structures,* vol. 232, p. 111183, 2021.

[50] R. Hill, "A self-consistent mechanics of composite materials," *Journal of the Mechanics and Physics of Solids,* vol. 13, no. 4, pp. 213-222, 1965.

[51] P. Vieville, A. Bonnet and P. Lipiński, "Modelling effective properties of composite materials using the inclusion concept. General considerations," *Archives of Mechanics,* vol. 58 , no. 3, pp. 207-239, 2006.

[52] A. Elmasry, W. Azoti, S. A. El-Safty and A. Elmarakbi, "A comparative review of multiscale models for effective properties of nano- and micro-composites," *Progress in Materials Science,* vol. 132, p. 101022, 2023.

[53] J. D. Eshelby, "The Determination of the Elastic Field of an Ellipsoidal Inclusion, and Related Problems," *Proceedings Mathematical Physical & Engineering Sciences,* vol. 241, no. 1226, pp. 376-396, 1957.

[54] A. Elmasry, W. Azoti and A. Elmarakbi, "Modelling and design of hierarchical fibre-graphene nanoplatelets reinforced elasto-viscoplastic polymer matrix composites to improve crashworthiness and energy absorption," *Composite Structures,* vol. 310, p. 116705, 2023.

[55] P. Zattarin, "Étude de l'intégration d'un modèle polycristallin dans un code d'éléments finis en élastoplasticité," 2000.

[56] B. Miled, I. Doghri, L. Brassart and L. Delannay, "Micromechanical modeling of coupled viscoelastic–viscoplastic composites based on an incrementally affine formulation," *International Journal of Solids and Structures,* vol. 50, no. 10, pp. 1755-1769, 2013.

[57] I. Doghri, Mechanics of deformable solids: Linear and nonlinear, analytical and computational aspects, Springer, 2000.

[58] I. Doghri, L. Adam and N. Bilger, "Mean-field homogenization of elasto-viscoplastic composites based on a general incrementally affine linearization method," *International Journal of Plasticity,* vol. 26, no. 2, pp. 219-238, 2010.

[59] "Standard Test Methods for Tension Testing of Metallic Materials [Metric] E 8M – 04," *ASTM International.*

[60] "Standard Test Method for Tensile Properties of Plastics D638 − 10," *ASTM International.*

[61] "Tensile Properties of Polymer Matrix Composite Materials D3039/D3039M − 14," *ASTM International.*

[62] "Standard Test Method for Flexural Properties of Polymer Matrix Composite Materials D7264/D7264M − 15," *ASTM International.*

[63] V. Mazzanti, R. Pariante, A. Bonanno, O. R. d. Ballesteros, F. Mollica and G. Filippone, "Reinforcing mechanisms of natural fibers in green composites: Role of fibers morphology in a PLA/hemp model system," *Composites Science and Technology,* vol. 180, pp. 51-59, 2019.

[64] S. Sathish, K. Kumaresan, L. Prabhu and N. Vigneshkumard, "Experimental investigation on volume fraction of mechanical and physical properties of flax and bamboo fibers reinforced hybrid epoxy composites," *Polymers & Polymer Composites,* vol. 25, no. 3, pp. 229-236, 2017.

[65] S. C. Das, A. D. L. Rosa, S. Goutianos and S. A. Grammatikos, "Flax fibers, their composites and application," in *Plant Fibers, Their Composites, and Applications*, J. Parameswaranpillai, S. Siengchin, T. Ozbakkaloglu and H. Wang, Eds., Elsevier, 2022, pp. 209-232.

[66] A. A. Vijayakumar, V. Prasad and M. K. Kochunny, "Investigation on the effect of stacking order and hybridization on mechanical and water absorption properties of woven flax/bamboo composites," *Polymer Composites,* vol. 43, no. 8, pp. 5189-5207, 2022.

[67] D. U. Shah, "Damage in biocomposites: Stiffness evolution of aligned plant fibre composites during monotonic and cyclic fatigue loading," *Composites Part A: Applied Science and Manufacturing,* vol. 83, pp. 160-168, 2016.

[68] C. Poilâne, Z. Cherif, F. Richard, A. Vivet, B. B. Doudou and J. Chen, "Polymer reinforced by flax fibres as a viscoelastoplastic material," *Composite Structures,* vol. 112, pp. 100-112, 2014.

[69] Z. Mahboob, Y. Chemisky, F. Meraghni and H. Bougherara, "Mesoscale modelling of tensile response and damage evolution in natural fibre reinforced laminates," *Composites Part B: Engineering,* vol. 119, pp. 168-183, 2017.

[70] G. Lebrun, A. Couture and L. Laperrière, "Tensile and impregnation behavior of unidirectional hemp/paper/epoxy and flax/paper/epoxy composites," *Composite Structures,* vol. 103, pp. 151-160, 2013.

[71] O. Akampumuza, P. M. Wambua, A. Ahmed, W. Li and X.-H. Qin, "Review of the Applications of Biocomposites in the Automotive Industry," *POLYMER COMPOSITES,* pp. 2553-2569, 2017.

[72] Dimitrios, Tzetzis, K. Tsongas and G. Mansour, "Determination of the Mechanical Properties of Epoxy Silica Nanocomposites through FEA-Supported Evaluation of Ball Indentation Test Results," *Materials Research,* vol. 20, no. 6, 2017.

[73] J. Essmeister, M. J. Taublaender, T. Koch, D. A. Cerrón-Infantes, M. M. Unterlass and T. Konegger, "High modulus polyimide particle-reinforcement of epoxy composites," *Materials Advances,* no. 7, 2021.

[74] M. Sajjad, B. Feichtenschlager, S. Pabisch, J. Svehla, T. Koch, S. Seidler, H. Peterlik and G. Kickelbick, "Study of the effect of the concentration, size and surface chemistry of zirconia and silica nanoparticle fillers within an epoxy resin on the bulk properties of the resulting nanocomposites," *Polymer International,* vol. 61, no. 2, pp. 274-285, 2011.

[75] I. Oral, H. Guzel and G. Ahmetli, "Determining the mechanical properties of epoxy resin (DGEBA) composites by ultrasonic velocity measurement," *journal of applied polymer science,* vol. 127, no. 3, pp. 1667-1675, 2013.

[76] D. B. Dittenber and H. V. GangaRao, "Critical review of recent publications on use of natural composites in infrastructure," *Composites Part A: Applied Science and Manufacturing,* vol. 43, no. 8, pp. 1419-1429, 2012.

[77] H. L. Bos, J. Müssig and M. J. v. d. Oever, "Mechanical properties of short-flax-fibre reinforced compounds," *Composites Part A: Applied Science and Manufacturing,* vol. 37, no. 10, pp. 1591-1604, 2006.

[78] M. Maier, A. Javadian, N. Saeidi, C. Unluer, H. K. Taylor and C. P. Ostertag, "Mechanical Properties and Flexural Behavior of Sustainable Bamboo Fiber-Reinforced Mortar," *Applied Sciences,* vol. 10, no. 18, 2020.

[79] G. R. Johnson and R. A. Stryk, "Eroding interface and improved tetrahedral element algorithms for high-velocity impact computations in three dimensions," *International Journal of Impact Engineering,* vol. 5, no. 1-4, pp. 411-421, 1987.

[80] T. Belytschko and J. I. Lin, "A three-dimensional impact-penetration algorithm with erosion," *Computers & Structures,* vol. 25, no. 1, pp. 95-104, 1987.

[81] M. Kabir, H. Wang, K. Lau and F. Cardona, "Chemical treatments on plant-based natural fibre reinforced polymer composites: An overview," *Composites Part B: Engineering,* vol. 43, no. 7, pp. 2883-2892, 2012.

[82] P. P. Das, A. Manral, F. Ahmad, B. Sharma, S. G. Vijay Chaudhary and P. Gupta, "Environmentally sustainable chemical treatment of plant fibers for improved performance of polymeric composites," *Polymer Composites,* vol. 43, no. 10, pp. 7155-7169, 2022.

[83] M. L. Sánchez, W. Patiño and J. Cárdenas, "Physical-mechanical properties of bamboo fibers-reinforced biocomposites: Influence of surface treatment of fibers," *Journal of Building Engineering,* vol. 28, p. 101058, 2020.

[84] H. Mason, "Natural fiber composites: Growing to fit sustainability needs," CompositesWorld, 27 March 2023. [Online]. Available:

https://www.compositesworld.com/articles/natural-fiber-composites-growing-to-fit-sustainability-needs.

[85] "Decarbonising the automotive industry with bamboo super fibres," Luxembourg institute of science and technology, 8 October 2023. [Online]. Available: https://www.list.lu/en/news/decarbonising-the-automotive-industry-with-bamboo-super-fibres/?no_cache=1&cHash=df43b0c5eee05364ad043d01846ca2e4.

[86] M. N. Baba, "Flatwise to Upright Build Orientations under Three-Point Bending Test of Nylon 12 (PA12) Additively Manufactured by SLS," *polymers,* vol. 14, p. 1026, 2022.

[87] Y. J. Nam, Y. K. Hwang, J. W. Park and Y. M. Lim, "CHAPTER 4: Fiber-Reinforced Cementitious Composite Design with Controlled Distribution and Orientation of Fibers Using Three-Dimensional Printing Technology," in *3D Concrete Printing: Construction and Building,* J. G. Sanjayan, A. Nazari and B. Nematollahi, Eds., Elsevier, 2019, pp. 59-72.

[88] L. Czechowski, J. Jankowski, M. Kotełko and M. Jankowski, "Experimental and Numerical Three-Point Bending Test for Sandwich Beams," *Journal of KONES Powertrain and Transport,* vol. 24, pp. 53-62, 2017.

934

935

**Declaration of interests**

☒ The authors declare that they have no known competing financial interests or personal relationships that could have appeared to influence the work reported in this paper.

☐ The authors declare the following financial interests/personal relationships which may be considered as potential competing interests: